Observation of the two-photon photoelectric effect in low-intensity optical fields during photostimulated fractal aggregation of colloidal silver

S. V. Karpov, A. K. Popov,[a] and V. V. Slabko
L. V. Kirenskiĭ Institute of Physics, Siberian Branch of the Russian Academy of Sciences, 660036 Krasnoyarsk, Russia;
Krasnoyarsk State Technical University, 660036 Krasnoyarsk, Russia

(Submitted 18 June 1997)
Pis'ma Zh. Éksp. Teor. Fiz. **66**, No. 2, 97–100 (25 July 1997)

The two-photon photoelectric effect enhanced by the characteristic local fields of fractal nanostructures is observed in optical fields with intensity of the order of 10^{-3} W/cm^2. © *1997 American Institute of Physics.* [S0021-3640(97)00614-2]

PACS numbers: 79.60.−i

The study of the rapid light-induced acceleration (by a factor of up to 10^{10}) of the growth of fractal aggregates (FAs) in silver hydrosols has produced spectroscopic indications that this is a photoemissive phenomenon.[1–3] This means that the rate of the photostimulated aggregation process should be determined by the magnitude of the photoemission current from the particles. The same conclusion was drawn in Ref. 4, where the increase in the rate of photocoagulation of Ag nanoparticles in aerosols was accompanied by an intensification of photoelectronic emission. In Ref. 5 these results are explained by the reciprocal heteropolar charging of particles of different size, which in turn is due to the size-dependence of the Fermi energy. This effect is manifested in the finite value of the electrical conductivity of the dispersion medium, whose equilibrium state can break down, for example, as a result the emission of photoelectrons under irradiation with light. We note that one (but not the only) possible photoemission mechanism of photoaggregation of sols was analyzed in Refs. 1 and 5.

In the present letter it is shown that photostimulated aggregation of nanoparticles in fractal structures in colloids is due to not only the one-photon but also the two-photon photoelectric effect even with irradiating light intensities of the order of the intensity of sunlight.

The degree of aggregation of the dispersed phase was monitored according to the absorption spectra of hydrosols. This method, which does not require a direct investigation of the structure of the aggregates with an electron microscope, is based on the results of Refs. 6, where the theory of the optical properties of fractal clusters is expounded. In these and subsequent works it is shown that a unique relationship exists between the structural and optical properties of the aggregates. The basic assumptions of this theory later found experimental confirmation in an entire series of works (see the references cited in Refs. 1–3).

In practice the degree of aggregation A of a colloid is determined from the broad-

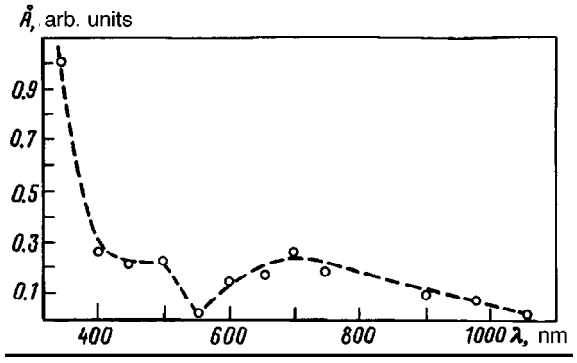

FIG. 1. Photostimulated aggregation rate $\dot{A}(\lambda)$ in a silver hydrosol versus the wavelength λ of the irradiating light in the range 360–1050 nm (the relative error equals 15%). The irradiation time equals 9.5 h and $I=3$ mW/cm^2.

ening of its absorption spectrum.[2,7] The limitations of this method do not extend to our experimental sols, with spherical particles and a small spread in sizes ($D\approx 5-18$ nm, with average diameter $\overline{D}=10$ nm). In our proposed approach the aggregation rate ($\dot{A}$) can be described by the change in the parameter A over a fixed exposure time (Δt): $\dot{A}=\Delta A/\Delta t$.

An investigation of the dependence of the photoaggregation rate $\dot{A}(\lambda)$ (with initial value $A=0$) on the wavelength of the irradiating light in the range 360–1050 nm (Fig. 1) established the red limit of this process, which ceases for $\lambda>\lambda_a=1050$ nm.[2] Furthermore, a deep intermediate minimum is observed in this dependence. This makes it possible to distinguish two parts in this dependence: The first one corresponds to the range 360–550 nm (I) and the second one corresponds to 550–1050 nm (II). The position of the intermediate minimum $\lambda_0=520-550$ nm is close to the experimental value of the red limit of the photoelectric effect for a metal–electrolytic-solution system, where this limit does not depend on the nature of the metal (in the case of an electrode photoelectric effect)[2,8] because of the screening action of the dense part of the electric double-layer. In this case, interestingly, the ratio λ_a/λ_0 equals approximately 2, i.e., photoaggregation appears in the range 550–1050 nm — beyond the red limit of the photoelectric effect — possibly because of the two-photon photoelectric effect.[2] The low efficiency of two-photon processes as compared with one-photon processes under weak illumination — of the order of $I=1-3$ mW/cm^2 — can be compensated by the contribution of a local field. This effect is due to a fundamental property of fractal aggregates — their capability (confirmed experimentally) of intensifying by many orders of magnitude the local electromagnetic fields.[6,9] The local-field (LF) enhancement factor is defined as $\Lambda=E_i/E$, the ratio of the local and external field intensities. Thus, in the case of Ag the field enhancement factor Λ_r for FAs at a frequency in resonance with the field increases from a factor of 250 in the 550–950 nm range up to a factor of 1300 and more as $\lambda=1050$ nm is approached.[2] According to Ref. 6, for aggregates this factor can be estimated according to equation $\Lambda_r=(\epsilon'-1)^2/\epsilon''$, where ϵ' and ϵ'' are the real and imaginary parts of the permittivity of the metal. Estimates show that for the characteristic experimental light intensities this results in the appearance of local fields ranging in intensity from several

hundreds up to several thousands of V/cm. These values are equivalent to a light intensity of the order of several tens of kW/cm^2. Such intensities, which are characteristic for laser pulses, are ordinarily adequate for observing two- and three-photon photoelectric effects (see, for example, Refs. 8 and 10).

In the theory of the n-photon electrode photoelectric effect the photocurrent density is described by the expression[10,2]

$$j_n = B(e^2/\hbar c)^{n-1}\omega_0^{1/2}(n\omega-\omega_0)^{5/2}\chi_n, \tag{1}$$

where χ_n is a function that depends on the properties of the metal and the interphase boundary in a specific system, $\chi_n \sim I^n$ (I is the radiation intensity), ω_0 is the frequency corresponding to the red limit of the photoelectric effect, B is a constant, e is the electron charge, $\hbar$ is the Planck constant, and c is the speed of light.

For a two-photon process the LF factor raised to the third power appears in expression (1) $j_2 \sim I^2 \sim \Lambda_r^3(\omega)E_i^4$, since according to Ref. 6 the exponent of Λ_r equals $n-1$, where n is the order of the nonlinear process. As a result of the fact that this exponent increases up to 3, the effect on j_2 of a rapid increase in $\Lambda_r^3(\omega)$ with decreasing frequency will be even more pronounced than in the case of the frequency dependence $\Lambda_r(\omega)$. For this reason, the two-photon photoelectric effect current j_2 increases rapidly with increasing radiation wavelength and estimates[2] show that in the range II it can reach values comparable to the one-photon photoemission current density in the near-threshold spectrum region for the same values of the intensity.

In the range II the character of the wavelength dependence $\dot{A}(\lambda)$ should be determined by the competition between the two spectral factors appearing in the expression for j_2. On the one hand, the function $(2\omega-\omega_0)^{5/2}$ monotonically approaches zero as the wavelength increases and as λ_a ($\omega_a = \omega_0/2$) is approached and, on the other hand, the cubed LF intensification factor $\Lambda_r^3(\omega)$, in contrast to the first function, increases rapidly as λ_a is approached. Since the ratios of the maximum and minimum values of the these two functions are approximately the same near the limits of the range II ($\Delta\lambda = 550-950$ nm), the product of the functions is described by a curve with a maximum.[2] The shape of this curve is qualitatively identical to the corresponding section of the experimental curve $\dot{A}(\lambda)$.

The deviations from a smooth power-law dependence $(\omega-\omega_0)^{5/2}$ in the region I can also be explained by taking account of the LF intensification factor, which increases from 25 ($\lambda = 400$ nm) up to 250 ($\lambda = 550$ nm). In this case, the wavelength dependence $\dot{A}(\lambda)$ is correlated in this range with the expression for $j_n(\omega)$ for $n=1$: $j_1 \sim \Lambda_r(\omega)E^2(\omega-\omega_0)^{5/2}$.

To identify the order of the photoemission process in the ranges I and II, the photoaggregation rate $\dot{A}(I)$ in identical samples of a typical silver hydrosol (based on collargol[2,3]) was investigated experimentally as a function of the intensity of the irradiating light with the same exposure times. The wavelength of the light was in the range I ($\lambda_1 = 450$ nm) in one case and in range II ($\lambda_2 = 700$ nm) in the other case. In accordance with expression (1), for the one- and two-photon photoelectric effects the photoemission current density behaves as $j_1 \sim I$ and $j_2 \sim I^2$, respectively. As one can see from Fig. 2, the

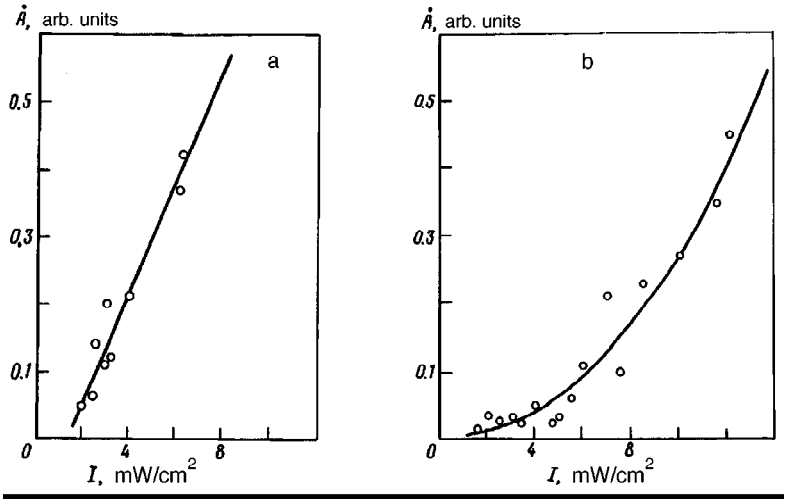

FIG. 2. a: Photostimulated aggregation rate $\dot{A}(I)$ in a silver hydrosol versus the intensity I of the irradiating light at $\lambda = 450$ nm with equal exposure times (2 h); b: same dependence obtained at $\lambda = 700$ nm with equal exposure times (4 h).

experimental curves $\dot{A}(I)$ obtained in these ranges are close to linear $\dot{A} \sim I$ (in the range I) and quadratic $\dot{A} \sim I^2$ (in the range II). Therefore these results together with the arguments presented above can serve as grounds for confirming the validity of the hypothesis that the photoemission in the range II is of a two-photon character.

We underscore that the enhancement of processes which are nonlinear functions of the field intensity by fractal nanostructures has been observed thus far only in nonlinear optical phenomena of the four-photon parametric scattering type (see, for example, Ref. 9).

We thank O. A. Kraev for participating in the experiments.

This work was supported by the Russian Fund for Fundamental Research (Grant No. 96-03-3434a).

[a)]e-mail: popov@cc.krascience.rssi.ru

[1] V. V. Slabko, S. V. Karpov, V. I. Zaitsev *et al.*, J. Phys.: Condens. Matter **5**, 7231 (1993).
[2] S. V. Karpov, A. L. Bas'ko, S. V. Koshelev *et al.*, Kolloid. Zh. **6** (1997).
[3] S. V. Karpov, A. K. Popov, V. V. Slabko *et al.*, Kolloid. Zh. **57**, 199 (1995).
[4] H. Burtscher and A. Schmidt-Ott, Phys. Rev. Lett. **48**, 25, 1734 (1982).
[5] É. L. Nagaev, Usp. Fiz. Nauk **162**(9), 49 (1992) [Sov. Phys. Usp. **35**, 747 (1992)].
[6] V. M. Shalaev and M. I. Shtokman, Zh. Éksp. Teor. Fiz. **92**, 509 (1987) [Sov. Phys. JETP **65**, 287 (1987)]; A. V. Butenko, V. M. Shalaev, and M. I. Shtokman, Zh. Éksp. Teor. Fiz. **94**, 107 (1988) [Sov. Phys. JETP **67**, 60 (1988)]; A. V. Butenko *et al.*, Izv. Akad. Nauk SSSR **53**, 1195 (1989).
[7] S. V. Karpov, A. K. Popov, and V. V. Slabko, Izv. Ross. Akad. Nauk, Ser. Fiz. **60**, 43 (1996).

[8] L. I. Korshunov, Ya. M. Zolotovitskiĭ, V. A. Benderskiĭ *et al.*, Usp. Khim. **XL,** 1511 (1971).
[9] S. G. Rautian, V. P. Safonov, P. A. Chubakov *et al.*, JETP Lett. **47**, 243 (1988).
[10] L. I. Korshunov, V. A. Benderskiĭ, V. I. Gol'danskiĭ *et al.*, JETP Lett. **7**(2), 42 (1968).

Translated by M. E. Alferieff

Explosive luminescence of silver azide

B. P. Aduev, É. D. Aluker, Yu. A. Zakharov, A. G. Krechetov, and I. V. Chubukin
Kemerovo State University,[a] 650043 Kemerovo, Russia

(Submitted 16 June 1997)
Pis'ma Zh. Éksp. Teor. Fiz. **66**, No. 2, 101–103 (25 July 1997)

Spectroscopic-kinetic investigations of the luminescence accompanying the explosive decomposition of silver azide are performed. A new phenomenon is observed: predetonation luminescence. A comparison of the predetonation luminescence spectrum with the band structure is in agreement with a model in which the exothermic reaction $2N_3^0 \rightarrow N_6$ provides the energy for the explosion. © *1997 American Institute of Physics.* [S0021-3640(97)00714-7]

PACS numbers: 82.40.Py, 78.55.Hx

Silver azide (AgN_3) has been for many years one of the main model objects in investigations of initiating explosives. However, the mechanism of the explosion of silver azide has remained unknown until recently. In Ref. 1 a new phenomenon was discovered: predetonation conduction in AgN_3, analysis of which showed unequivocally that the explosion occurs by a chain mechanism. It was also noted in Ref. 1 that intense luminescence is present even before mechanical breakup of the sample occurs. In the present work we investigated the spectroscopic–kinetic characteristics of this luminescence. It seemed to us that such a study should shed light on the nature of the chain process.

The objects of investigation were $3\times3\times0.05$ mm AgN_3 single crystals grown from solution. The explosion was initiated by a pulse from an electron accelerator (3 ns, 400 keV, 100–1000 A/cm^2). An ISP-51 spectrograph performed a spectral decomposition of the luminescence from a specimen placed in a vacuum chamber. The image of the spectrum was focused on the time slit of the image converter (IC) of a FÉR-7 photoelectric recorder (time resolution 2 ns, spectral range 40–1000 nm). A readout unit based on a silicon intensifier target tube digitized the output signal from the FÉR-7 recorder and stored the digitized signal in a computer, where corrections were made to the spectral sensitivity and the band characteristic of the measuring channel.

The results of an analysis of a typical IC diagram (wavelength and time sections) are displayed in Fig. 1. Here two types of luminescence are clearly distinguished (Fig. 1a): wide-band prebreakup luminescence of the specimen — predetonation luminescence ($t_1\approx0.5$ μs, Fig. 1b) and a line spectrum of the plasma produced by the explosion ($t_2\approx2.5$ μs, Fig. 1c). It should be noted that the time interval between the predetonation luminescence and the appearance of a plasma line spectrum fluctuates from one specimen to another. An identification of the lines in the plasma spectrum is presented in Fig. 1c.

The wide-band solid-state luminescence is of the main interest from the standpoint of the problem addressed in this work (Fig. 1b). This luminescence spectrum cannot be

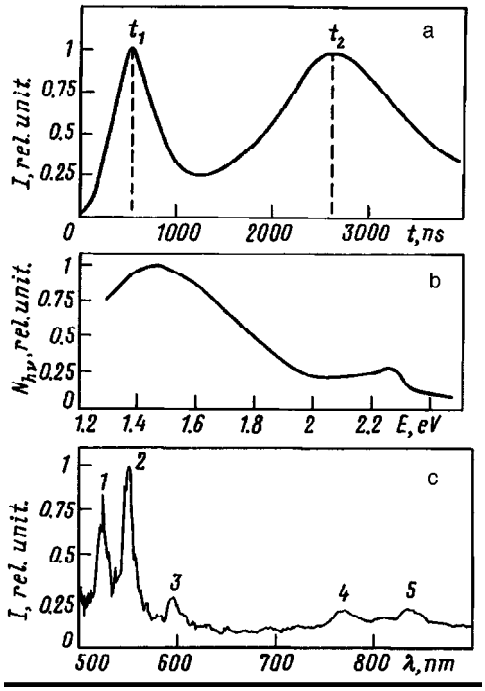

FIG. 1.

described by the Planck formula, i.e., it is not thermal emission and can be identified definitely as predetonation luminescence. The fall-off of the predetonation luminescence intensity before the appearance of the plasma luminescence (Fig. 1c) is apparently due to reabsorption by itinerant electrons and holes. Indeed, according to the data of Ref. 1, in the solid-phase chain reaction process the itinerant charge-carrier density in the crystal reaches values $>10^{20}$ cm^{-3} corresponding to absorption coefficients of the order of 10^3-10^2 cm^{-1},[2] which result in substantial absorption of the luminescence signal.

At extremely high itinerant charge-carrier densities ($>10^{20}$ cm^{-3}) all forms of luminescence associated with biographic defects saturate.[2] For this reason, the observed luminescence could be due to only fundamental radiative transitions or transitions with the participation of defects generated directly during the chain reaction. Comparing the predetonation luminescence spectra with the band structure of AgN_3 (Ref. 3) shows that the predetonation luminescence is not related with interband and valence–core transitions (cross luminescence). The intraband luminescence yield is extremely low.[4] Therefore it is most likely that the predetonation luminescence is associated with defects formed during the chain reaction.

The following model of an elementary event in the chain reaction in AgN_3 was proposed in Ref. 5. In the case when two holes (N_3^0 radicals) are localized on a defect a reconstruction of the defect occurs as a result of the exothermic reactions $2N_3^0 \rightarrow N_6$ (4–6 eV) or $2N_3^0 \rightarrow 3N_2$ (8–10 eV), leading to the appearance of a quasilocal state (hole center)

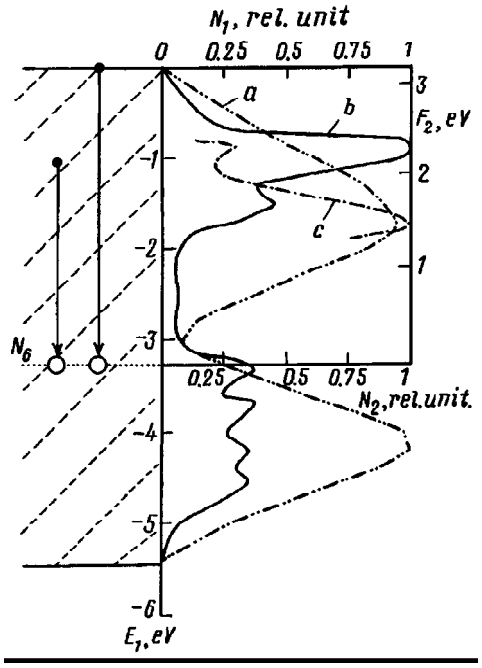

FIG. 2.

whose level lies in the valence band (2–3 eV from the band top in the case $2N_3^0 \rightarrow N_6$ and 4–5 eV in the case $2N_3^0 \rightarrow 3N_2$).

According to this model, hole multiplication, which is a necessary condition for the development of a chain reaction, occurs as a result of impact ionization by holes delocalized from this center.

A comparison of the predetonation luminescence spectrum with the density of states in the AgN_3 valence band (Fig. 2) shows fairly good agreement with the model proposed in Ref. 5 for the case $2N_3^0 \rightarrow N_6$.

[a)]e-mail: rk@rk.uucp.stanet.ru

---

[1]B. P. Aduev, É. D. Aluker, G. M. Belokurov, and A. G. Krechetov, JETP Lett. **62**, 215 (1995).
[2]É. D. Aluker, V. V. Gavrilov, R. G. Deĭch, and S. A. Chernov, *Fast Radiation-Stimulated Processes in Alkali-Halide Crystals* [in Russian], Zinatne, Riga, 1987.
[3]A. B. Gordienko, Ju. N. Zhyravlev, and A. S. Poplavnoi, Phys. Status Solidi B **198**, 707 (1996).
[4]É. D. Aluker, V. V. Gavrilov, R. G. Deĭch, and S. A. Chernov, JETP Lett. **47**, 142 (1988).
[5]B. P. Aduev, É. D. Aluker, G. M. Belokurov, and A. G. Krechetov, Izv. Vyssh. Uchebn. Zaved. Fiz. **11**, 162 (1996).

Translated by M. E. Alferieff

Role of the parameters of external fields acting on a spin system in harmonic-generation processes

I. I. Sadykov
Kazan State University, 420008 Kazan, Russia

(Submitted 10 June 1997)
Pis'ma Zh. Éksp. Teor. Fiz. **66**, No. 2, 104–109 (25 July 1997)

Crossed dc and ac magnetic fields are applied to a paramagnet in a continuous regime in an investigation of the induction signal at the doubled and tripled pump frequencies. The experimental object is powdered diphenyl picryl hydrazyl (DPPH), and the pump frequency used is 11 MHz. It is shown that harmonic generation and the orientational dependences of the harmonics arise due to nonlinear variations of the magnitude and the ''rocking'' angle of the vector sum of the external fields and the precession frequency of the spin magnetization. Anomalies are observed in the Bloch–Siegert effect. © *1997 American Institute of Physics.* [S0021-3640(97)00814-1]

PACS numbers: 42.65.Ky, 75.25.+z

There are many publications concerning multiquantum resonance effects. Second-harmonic generation by a spin system was investigated experimentally and theoretically in Ref. 1. Resonance was observed at two values of the external static magnetic field H_z $H(1)=\omega_p/\gamma$ and $H(2)=2\omega_p/\gamma$, where ω_p is the pump frequency and γ is the gyromagnetic ratio. Reference 2 reports the results of investigations of weak-field multiquantum resonances by optically detected ESR from radical–ion pairs. Observational results are presented not only for the first two resonances but also for a third resonance, i.e., $H(3)=3\omega_p/\gamma$. Harmonic generation can be described theoretically by a quantum-mechanical approach[1–3] or by the quasiclassical approach proposed by Bloch.[4] In the first case there are problems in determining the order of the approximation, especially when the amplitude H_m of the ''perturbing'' ac field is comparable to or even less than the static field H_z. Ordinarily, the ac field is oriented along the x axis, and its component $H_x(t)=H_m\cos(\omega_p t)$. In the second case the initial phenomenological Bloch equations also make it possible to calculate the harmonic components and their orientational dependences,[5] but they can be correct only if $H_m \ll H_z$. The expected values of the spectroscopic parameters — the intensities, moments, and shapes of the resonance lines as well as the shifts of these lines due to the Bloch–Siegert effect (BSE) — can be calculated in the approximations of both methods.[6,7] In particular, the quantum approach predicts that the line broadening and line shifts as functions of H_m are different for two- and three-quantum transitions. As far as we know, these effects have never been checked experimentally. Furthermore, although quite intense pump fields, sufficient for observing line broadening and line shifts, were employed in Refs. 1 and 2, the authors make no mention of this and do not discuss this question. To compare the theory and experiment correctly it is necessary to investigate experimentally the parameters not only of the

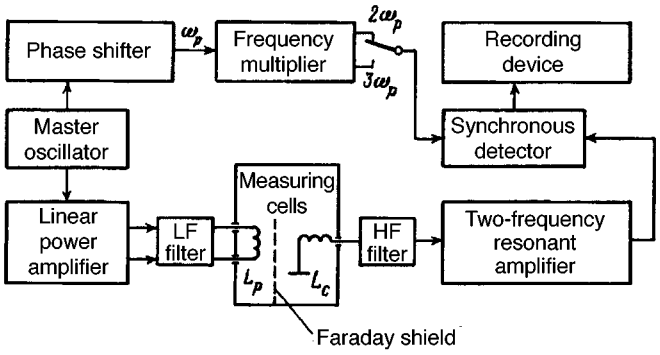

FIG. 1. Bloch diagram of the spectrometer.

second harmonic but also of at least the third harmonic, all harmonics being radiated in the same manner. In so doing, the ratio H_m/H_z should be adequate for measuring the BSE reliably. Our aim in the present work was to solve these problems.

A coherent spectrometer with crossed coils was developed for obtaining the experimental results. A block diagram of the spectrometer is displayed in Fig. 1. As one can see, the overall scheme is similar to that of the first-generation high-resolution spectrometers,[8] but there are a number of substantial differences. First, signals not at the first harmonic but rather at the second and third harmonics are amplified and detected. Second, a linear power amplifier, a low-frequency filter, and a Faraday shield (to reduce to a minimum the parasitic interferences which unavoidably arise in the generator and power amplifier circuit at the frequency of the detected signal and penetrate into the measuring cell) are employed. The detecting coil L_c consists of two saddle-shaped halves and is placed inside a cylindrical coil L_p and a Faraday shield is placed between these coils. The high-frequency filter is necessary to prevent the residual high-frequency pump voltage from reaching the input cascade of the two-frequency amplifier. The constant field H_z, orthogonal to the field H_x, is produced by Helmholtz coils (not shown in the diagram) and can be oriented at an angle β relative to the axis of the receiving coil L_c. The spectrometer parameters were as follows: $\omega_p/2\pi = 11$ MHz, $H_z = (-60)-(+60)$ Oe, $H_m = 2-12$ Oe, and $\beta = (-180°)-(+180°)$. The nonuniformity of the fields at the center of the coils in a sample of volume 0.4 cm^3 does not exceed 2% for H_x and 0.5% for H_z. The level of the parasitic interference in both channels also does not exceed the average experimental signal level, and in the absence of a pump field H_x the possible ESR signal from these interferences is not observed even at maximum gain. The value of H_z was measured according to the positions of the ESR lines at the harmonic frequencies and the amplitude H_m was calibrated by an induction method and according to the BSE. Powdered polycrystalline diphenyl picryl hydrazyl (DPPH) — the most extensively studied paramagnet with a single, narrow ESR line[1,9] — was chosen as the object of investigation. The experimental results are displayed in Fig. 2 (solid curves). As one can see, quite sharp resonances $R(m,n)$, which are symmetric in the field H_z and are antisymmetric in magnitude, are observed at both harmonics. Here m enumerates the resonances appearing with increasing field H_z and n enumerates the harmonics by means of which the reso-

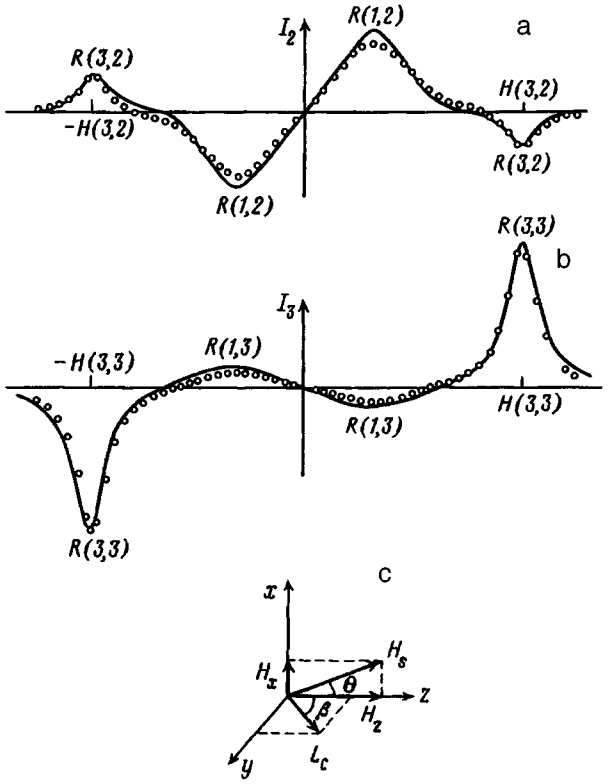

FIG. 2. Traces of the signal intensities from DPPH (solid curves) of mass 0.16 as a function of H_z with fixed $H_m = 4.8$ Oe: a — Sine component of the second-harmonic signal (I_2) with $\beta = 0$; b — cosine component of the third-harmonic signal (I_3) with $\beta = \pi/2$; c — relative orientations of the fields H_x and H_z and the axis of the detecting coil L_c (the scale is 1.4 times smaller than for I_2). The dots show the numerical results, obtained on the basis of Eqs. (7), for I_2 and I_3 for the same conditions and $T_1 = T_2 = 6.3 \times 10^{-8}$ s. The resonance values of the field are $H(3,2) = H(3,3) = \pm 10.25$ Oe.

nances are recorded. In this notation, the classical ESR can be represented as $R(1,1)$. It is easy to see from the curves a and b (Fig. 2) that the resonances $R(1,2)$ and $R(1,3)$ have approximately the same but strongly broadened line shape. The positions of the maxima of these resonances are determined, to a first approximation, by a somewhat modified Bloch–Siegert relation

$$H_{R1} = H_{R(1,n)}\{1 + [H_m / kH_{R(1,n)}]^2\}. \tag{1}$$

Here $H_{R1} = \omega_p / \gamma$ is the resonance value of the field H_z for $H_m \ll H_{R1}$, $H_{R(1,n)}$ is the resonance value of the field H_z for fixed H_m, γ is the gyromagnetic ratio, and $k = 4$.

The second resonance $R(2,2)$ observed in Ref. 1 is weak in our experiments, and we shall not discuss it in the present letter. The third resonances $R(3,2)$ and $R(3,3)$ are broadened much less than the first resonances but undergo a much stronger dynamic shift and are determined, to a first approximation, by the equation (1) but with $k = 2$. This fact

can be interpreted as an anomalous BSE. On the whole, the intensities of the resonances depend on the angle as $\cos\beta$ at the second-harmonic frequency and as $\sin\beta$ at the third-harmonic frequency. Analysis shows that our experimental results cannot be completely described either by quantum-mechanical calculations in the approximations of Refs. 1 and 2 or by the Bloch equations.[4] We were able to solve this problem qualitatively and semiquantitatively by the phenomenological system of Bloch-type differential equations presented below. These equations were obtained with the following assumptions and approaches. According to Fig. 2c the fields H_x and H_z give a field of magnitude

$$H_s=\sqrt{H_z^2+H_x^2(t)}, \tag{2}$$

and angle of inclination from the axis of equilibrium (the z axis)

$$\theta=\tan^{-1}(H_x(t)/H_z). \tag{3}$$

Therefore the total vector $H_s(t)$ ''rocks'' with frequency ω_p in a sector bounded by the angles $\pm\theta_{\max}=\tan^{-1}(H_m/H_z)$. For clarity, we note that in obtaining the curves a and b in Fig. 2 this angle varies from ± 90 to ± 22 degrees. The fact that the precession frequency and direction of the macroscopic magnetization of the paramagnet will be determined by the magnitude and direction of this rocking field evidently requires no special proof.[5] Then we can write

$$\omega_s=\gamma\cdot H_s\,. \tag{4}$$

We shall not follow the usual practice of switching to a rotating coordinate system. Rather, we shall confine ourselves to the rocking coordinate system and describe the behavior of the magnetization m in this system in the form of the trial functions

$$m_x=m_0\,\cos(\omega_s t)\exp(-t/T_2), \tag{5a}$$

$$m_y=m_0\,\sin(\omega_s t)\exp(-t/T_2), \tag{5b}$$

$$m_z=M_s[1-\exp(-t/T_2)]. \tag{5c}$$

These functions are solutions of the system of Bloch differential equations, except that the stationary magnetization and Larmor frequency are replaced by their dynamic parameters $M_s=\chi\cdot H_s$ and ω_s, respectively. Here χ is the static magnetic susceptibility. Further, the components of the magnetization $M_{x,y,z}$ in the laboratory coordinate system can be represented by the projections $m_{x,y,z}$ and vice versa, taking account of the angle θ, as

$$\begin{aligned} M_x&=m_x\,\cos\,\theta+m_z\,\sin\,\theta,\\ M_y&=m_y\,,\\ M_z&=-m_x\,\sin\,\theta+m_z\,\cos\,\theta, \end{aligned} \tag{6a}$$

$$\begin{aligned} m_x&=M_x\,\cos\,\theta-M_z\,\sin\,\theta,\\ m_y&=M_y\,,\\ m_z&=M_x\,\sin\,\theta+M_z\,\cos\,\theta. \end{aligned} \tag{6b}$$

Differentiating Eq. (6a) with respect to time, making the substitutions (6b), and performing the appropriate elementary trigonometric and algebraic transformations, we arrive at a system of differential equations. To simplify the equations we represent them in the matrix form

$$dM_i/dt=\sum_{i,l}\ (A_{il}M_l+B_i)_{i,l=x,y,z}\,. \tag{7}$$

Here

$$A_{xx}=-(\sin^2\ \theta/T_1+\cos^2\ \theta/T_2),$$

$$A_{yy}=-1/T_2,\quad A_{zz}=-(\sin^2\ \theta/T_2+\cos^2\ \theta/T_1),$$

$$A_{xy}=-A_{yz}=\omega_s\ \sin\ \theta,$$

$$A_{xz}=A_{zx}=(1/T_2-1/T_1)\sin\ \theta\ \cos\ \theta,$$

$$B_x=M_s\ \sin\ \theta/T_1,\quad B_y=0,\quad B_z=M_s\ \cos\ \theta/T_1,$$

$$M_s=\chi\cdot H_s,$$

and T_1 and T_2 are the spin-lattice and spin-spin relaxation times, respectively.

The derivation of Eqs. (7) also assumed that the quantities M_s, ω_s, and θ do not change in the time interval dt and therefore their derivatives equal zero. It is easy to show that Eqs. (7) obtained above become the Bloch equations (Ref. 4) when $H_m \ll H_z$. The results obtained by numerically solving the system of equations (7) and then differentiating each M_i and expanding the obtained results in a Fourier series with one period $T_p=2\pi/\omega_p$, corresponding to the time $t=nT_p>T_1+T_2$, in terms of the harmonics are presented in Fig. 2 (small circles). Here n is an integer. The differentiation is necessary because the emf induced in the detecting coil is determined not by the magnetization components themselves but rather by their derivatives.[8] A comparison shows that the experimental results agree qualitatively with the numerical calculations. The quantitative accuracy of the approximation can be increased by varying the relaxation times T_1 and T_2 more carefully. However, then there arises the situation $T_1<T_2$, which contradicts the well-known and theoretically well-established necessary condition $T_1\geqslant T_2$ (Ref. 10). Equations (7), like the Bloch equations, can describe only Lorentzian resonance lines. It is well known[11] that the DPPH ESR line shape falls between a Lorentzian and a Gaussian. This contributes to the approximation error. As far as the BSE is concerned, in this case there is qualitative and quantitative (to a first approximation) agreement between the calculations and the experimental results. The dependences of the computed intensities of the resonances on the orientational angle β also agree well with experiment. Furthermore, calculations were performed for the expected harmonics from the first to the fourth. These calculations showed that the even harmonics are maximum for $\beta=0$ and vanish for $\beta=\pi/2$ and, conversely, the odd harmonics are maximum for $\beta=\pi/2$ and vanish for $\beta=0$. These deficiencies of Eqs. (7) can be attributed to the effects of the second-order approximation and can possibly be eliminated by further elaborating the theoretical approach proposed in Ref. 12.

The following conclusions can be drawn from an analysis of the experimental and theoretical results obtained. The phenomenological equations (7) give a classical description of the dynamics of the nonlinear motion of the measured physical quantity — the macroscopic magnetization. Therefore it can be assumed, at least for a system with effective spin 1/2, which DPPH is, and taking the relation (4) into account, that there are no more than two magnetic quantum levels in the rocking coordinate system and a selection rule with a change in the magnetic quantum number by ± 1 ($\Delta m = \pm 1$) operates. In other words, one-quantum processes predominate at the microscopic level and, on account of the nonlinear external parameters H_s and θ and also the internal parameter ω_s, the nonlinear motion of the spin magnetization give rise to the generation and orientational dependences of the harmonics.

This stage of the work was supported by the Kazan Physical Society. I am grateful to V. N. Efimov for assisting in the experiments, M. L. Laryukhin and S. S. Sakhovskiĭ for assisting in the calculations, and B. M. Kazakov, R. V. Saburova, and N. K. Solovarov for helpful discussions.

[1] R. Boscaino, I. Ciccarello, C. Cusumano, and M. W. P. Strandberg, Phys. Rev. B **3**, 2675 (1971).
[2] V. A. Morozov, O. N. Antzutkin, A. V. Koptyug, and A. B. Doktorov, Mol. Phys. **73**, 517 (1991).
[3] S. Yatsiv, Phys. Rev. **113**, 1522 (1959).
[4] F. Bloch, Phys. Rev. **70**, 460 (1946).
[5] A. Abragam, *The Principles of Nuclear Magnetism*, Clarendon Press, Oxford, 1961 [Russian translation, IL, Moscow, 1963].
[6] F. Bloch and A. Siegert, Phys. Rev. **57**, 522 (1940).
[7] D. T. Pegg, J. Phys. B **6**, 246 (1973).
[8] A. Lösche, *Kerninduktion*, VEB, Berlin, 1957 [Russian translation, IL, Moscow, 1963].
[9] V. A. Atsarkin, G. A. Vasneva, and V. V. Demidov, Zh. Éksp. Teor. Fiz. **108**, 927 (1995) [JETP **81**, 509 (1995)].
[10] I. V. Aleksandrov, *Theory of Magnetic Relaxation* [in Russian], Nauka, Moscow, 1975.
[11] C. P. Poole, *Electron Spin Resonance: A Comprehensive Treatise on Experimental Techniques*, Interscience, New York, 1967 [Russian translation, Mir, Moscow, 1970].
[12] I. K. Vaganov, Zh. Éksp. Teor. Fiz. **70**, 657 (1976) [Sov. Phys. JETP **43**, 339 (1976)].

Translated by M. E. Alferieff

Identification of the polymerized orthorhombic phase of C_{60} fullerene

V. A. Davydov,[a] L. S. Kashevarova, and A. V. Rakhmanina
L. F. Vereshchagin Institute of High-Pressure Physics, Russian Academy of Sciences, 142092 Troitsk, Moscow District, Russia

A. V. Dzyabchenko
Karpov Physicochemical Institute, 103064 Moscow, Russia

V. N. Agafonov, P. Dubois, and R. Ceolin
Laboratoire de Chimie Physique, JE 408, Faculté de Farmacie, 37200 Tours, France

H. Szwarc
Laboratoire de Chimie Physique des Materiaux Amorphes, Universite Paris Sud, 91405 Orsay, France

(Submitted 19 June 1997)
Pis'ma Zh. Éksp. Teor. Fiz. **66**, No. 2, 110–114 (25 July 1997)

It is established by x-ray diffraction and Raman scattering that the polymerization of C_{60} fullerene at 1.5 GPa and 723 K leads to the formation of an orthorhombic phase that is different from the previously identified high-pressure orthorhombic phase. It is determined by a calculation of the optimal packing of linear C_{60} polymers by the method of atom–atom potentials that the energetically favorable structure of the orthorhombic phase belongs to the space group $Pnnm$ and not the previously proposed group $Immm$. The computed value of the rotation angle of the polymer chains that corresponds to the minimum packing energy was equal to 61°. The mechanisms leading to the formation of the polymerized phases are discussed on the basis of the results obtained.
[S0021-3640(97)00914-6]

PACS numbers: 61.48.+c, 81.15.Tv

The study of transformations of C_{60} fullerene at high pressures and temperatures has shown that the identification of the different carbon states formed in the system presents certain difficulties.[1–8] In Ref. 4 we proposed a scheme for classifying the carbon states that form under nonhydrostatic compression of C_{60} fullerite at pressures up to 10 GPa and temperatures up to 1900 K. Using the character of the structure-forming element (atom, molecule, polymolecular cluster) as a criterion, different types of carbon states were distinguished in the system: molecular, polymolecular (polymerized and polycondensed), and atomic. We performed a x-ray phase analysis of the polymerized states (PSs) on the basis of the phase identification made in Ref. 1. In the present letter we report experimental and model computational results that make it possible to refine the previously obtained data on the identification of PSs.

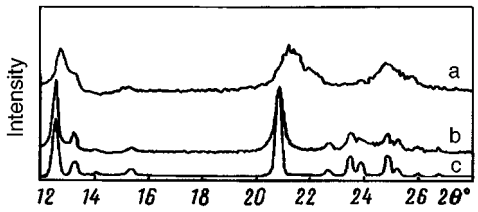

FIG. 1. Experimental OHPP diffraction pattern (a) and the experimental (b) and computed (c) OLPP diffraction patterns.

The experimental part consisted of the synthesis of C_{60} PSs with different p, T-parameters and the segregation of the states under normal conditions by quenching under pressure, followed by x-ray diffraction and Raman scattering analysis. Fullerite powder with 99.9 mol.% C_{60}, produced by the Term USA Company, was used as the starting material. The fullerite was treated in ''piston–cylinder'' and ''toroid'' type high-pressure chambers. The details of the synthesis of the PSs are described in Ref. 4. The diffraction patterns of the powdered samples were obtained with a Siemens D500 diffractometer in CoK_α radiation. A Bruker FT Raman RFS100 spectrometer with 1064 nm excitation radiation was used to study the Raman scattering spectra.

As mentioned in Ref. 4, we identified, on the basis of the fact that our diffraction patterns were identical to those obtained in Ref. 1, the series of PSs which form at pressures of 2–10 GPa and temperatures below 673 K as an orthorhombic (O) phase, first identified at 8 GPa and 573 K,[1] and then in the entire pressure range 4–8 GPa and temperatures $\sim 473-573$ K.[7] Later[8] it was established that an O phase with lattice parameters different from those proposed in Ref. 1 exists in the samples synthesized at 1.5 GPa and 723 K. The observation of two O phases in the system — conventionally, an orthorhombic high-pressure phase (OHPP) and an orthorhombic low-pressure phase (OLPP) — made it necessary to study these two states of the system in greater detail.

Figures 1 and 2 display x-ray diffraction patterns and Raman scattering spectra of samples obtained at 8 GPa and 573 K (OHPP) and at 1.5 GPa and 723 K (OLPP). As one

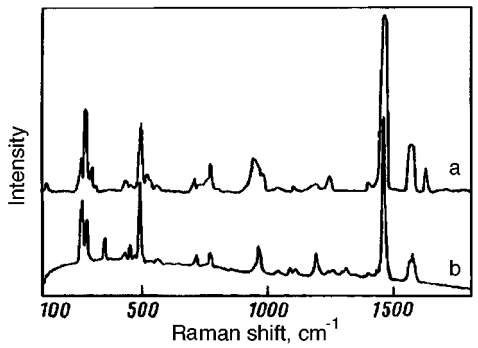

FIG. 2. OHPP (a) and OLPP (b) Raman spectra.

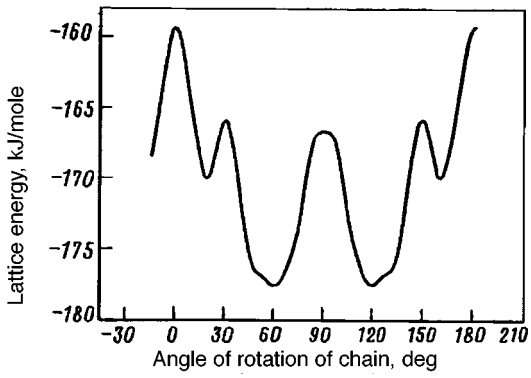

FIG. 3. Energy of a polymerized-OHPP crystal lattice as a function of the rotation angle of a polymer chain around its axis.

can see from Fig. 1, the OLPP diffraction pattern contains a larger number of peaks and the peaks themselves are much narrower. The indexing of the OLPP diffraction pattern over 11 well-resolved peaks performed with the DICVOL-91 program[9] gave an orthorhombic body-centered ($Immm$) cell with the parameters $a=0.9098(6)$, $b=0.983(1)$, and $c=1.472(2)$ nm and two C_{60} molecules. The computed diffraction pattern (Fig. 1c), constructed with the LAZY ROUTINE program on the basis of the polymer-chain geometry proposed in Ref. 10, showed satisfactory agreement with the experimental curve, confirming the correctness of the values obtained for the lattice constants. However, an attempt to determine on the basis of the experimental data the polymer-chain orientations which are the result of a rotation of a chain around its axis and which change the space group from $Immm$ to $Pnnm$ in the case when the angle of rotation is different from 0 or 90° did not give a definitive result. This failure is due to the quality of the sample, which did not permit obtaining a diffraction pattern with a large number of well-resolved diffraction peaks, and the insensitivity of the diffraction pattern to a rotation of the chains.

For this reason, to clarify the space group of the OLPP the optimal packing of polymer chains was calculated by the atom–atom potentials method using the PMC (packing of molecules in crystals) program.[11] In the calculation, the energy of the crystal structure calculated using an empirical intermolecular potential was minimized with respect to the structural parameters of the OLPP. In so doing, the geometry of the polymer chain was assumed to be given and the distance between the centers of neighboring molecules in a chain was taken as the short period of the OLPP lattice, taken from the x-ray experiment. The intermolecular potential was calculated as the sum of Lennard–Jones type atom–atom potentials, which are responsible for the van der Waals interaction of the carbon atoms, and the Coulomb interactions of the effective positive and negative charges located at the midpoints of the single and double carbon–carbon bonds, respectively. The computational problem was to determine the rotation angle corresponding to the optimal packing of the chains. It was found that the energetically most favorable packing is the one with a rotation angle of 61°, i.e., $Pnnm$ symmetry (Fig. 3). In this case a cell contains two chain orientations related by a mirror reflection operation. This is in contrast to the $Immm$ group, for which all chains have the same orientation. For close

lattice parameters, obtained in a calculation of two types of single-orientation structural models ($Immm$ — rotation angles of 0 and 90°) and a double-orientation structural model ($Pnnm$ — rotation angle 61°), the energy gain in the latter case equals about 18 and 10.5 kJ/mole, respectively. Therefore, although the quality of the experimental OLPP diffraction patterns obtained with powder does not permit a definitive choice of an orientational model of the structure, the model calculation points to $Pnnm$ as the preferred packing.

The data presented in Fig. 1 show that the OLPP diffraction pattern differs substantially from the OHPP diffraction pattern, which, according to Ref. 1 is also indexed in the orthorhombic ($Immm$, $Z=2$) cell with the parameters $a=0.926$, $b=0.988$, and $c=1.422$ nm. However, identifying as individual O phases the PSs obtained at 8 GPa and 573 K,[1] and 4.8 GPa and 523 K,[7] raises some doubts.

First, as was noted in Ref. 8, on account of the large width and the small number of clearly distinguished diffraction peaks the OHPP diffraction pattern can be indexed with the same qualitative indicators in both orthorhombic and rhombohedral cells. The difficulty of identifying as an O phase the OHPP-like PSs was actually also noted in Ref. 2, where an attempt was made to describe them as a rhombohedral (R) phase, though in the final variant it was represented as a fcc(pC_{60}) phase — a face-centered high-pressure cubic phase — despite the problems of such an indexing also, as were noted by the authors themselves.

It is interesting that in the case of an OHPP the short lattice period, which in structural models of the O phase equals the distance between the centers of neighboring molecules in a polymer chain, is much larger than the theoretically computed distances between the C_{60} molecules in a linear polymer — 0.9127,[12] 9.11,[13] and 0.906 nm.[14]

The character of the splitting of the Hg(1) mode, the presence of lines at 523, 535, 1402, 1449, and 1620 cm^{-1} in the OHPP Raman spectrum (Fig. 2), and a number of other features of the spectrum that are characteristic of two-dimensionally polymerized states also attest to the fact that linear C_{60} molecules are not the only structure-forming elements of the OHPP.

The ambiguity of the interpretation of the diffraction patterns of the PSs obtained under pressure at relatively low temperatures $\sim$323–573 K can be explained by assuming that these PSs are still not completely formed polymerized phases (PPs) with a definite type of crystal lattice, as are clearly seen in the case of synthesis temperatures above 573 K, but rather they are some intermediate states with a low degree of three-dimensional ordering.

The O-phase representation of PSs formed at pressures up to 8 GPa and temperatures of 373–573 K served as a basis for the suggestion of the mechanism in which 2 + 2 cycloaddition reactions between linear C_{60} polymers lead to the formation of layered tetragonal T and R phases.[7] For the T phase such a formation mechanism cannot be excluded in principle even though the mechanism requires the energetically unfavorable $Immm$ packing for the O phase, since otherwise ($Pnnm$ packing with a rotation angle different from an angle between 0 and 90°) the double bonds entering in the 2 + 2 cycloaddition reaction are located far from one another or are not parallel. For the R phase, however, this formation mechanism is virtually impossible, since in this case even

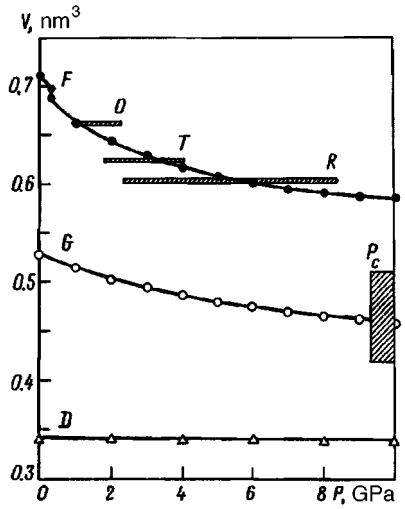

FIG. 4. Compression isotherms of fullerite C_{60} (F),[15] graphite (G),[16] and diamond (D)[17] at 298 K and volumes per C_{60} molecule, taken for normal conditions of polymolecular crystalline OLPP (O), T and R phases, and amorphous P_c states of a system which form under different pressures in the temperature range 573–1073 K.

the *Immm* packing of the O phase does not meet the necessary conditions for the appearance of interchain bonds. This suggests the presence of a mechanism leading to the formation of T and R phases that is associated with the direct two-dimensional polymerization of C_{60} molecules and is based on the assumption that at high pressures there exists a series of molecular packings of C_{60} which appear as molecular precursors of the observed PSs and are characterized by a favorable (from the standpoint of the formation of two-dimensional structure-forming elements of these phases) relative arrangement of the double bonds of neighboring molecules. We have not yet been able to observe such hypothetical molecular precursors of PPs experimentally, but the first attempts to simulate them by numerical calculations show that they could indeed exist. A comparative analysis of the volumes of the PPs and the molecular states subjected to compression suggests that the proposed mechanism of the formation of PPs is possible (Fig. 4). The dimensions of the rectangles in Fig. 4 characterize the range of synthesis pressures and the range of volumes of the corresponding states of the system that we obtained with different synthesis temperatures. One can see from Fig. 4 that the volumes of the molecular states of the system, which are compressed at 298 K, are correlated with the PPs which form when the compressed states are heated above 573–673 K at a fixed pressure. Since the experimental procedure for synthesizing the high-pressure phases ordinarily consists of loading a sample up to prescribed pressures at room temperature and then heating the sample under a fixed load, it can be conjectured that in this case heating the system ''only'' activates the PP formation process, while the pressure acting on the system at the moment preceding heating is the factor that determines the type of phase formed. Specifically, if the volume of the C_{60} molecular crystal compressed at 1.5 GPa and 298 K is virtually identical to that of the OLPP, then the main PP formed at 1.5 GPa and 723 K is obviously an OLPP. According to this scheme, the molecular state at 8 GPa

and 298 K is the molecular precursor of a rhombohedral and not an orthorhombic phase.

This work was supported by the Russian Fund for Fundamental Research (Grants Nos. 97-03-33584a and 95-03-09418) and INTAS (Grant No. 93-2133).

[a)]e-mail: vdavydov@ns.hppi.troitsk.ru

[1] M. Nunez-Regueiro, L. Marques, J.-L. Hodeau *et al.*, Phys. Rev. Lett. **74**(2), 278 (1995).
[2] Y. Iwasa, T. Arima, R. M. Fleming *et al.*, Science **264**, 1570 (1994).
[3] I. O. Bashkin, V. I. Rashchupkin, A. F. Gurov *et al.*, J. Phys.: Condens. Matter **6**, 7491 (1994).
[4] V. A. Davydov, L. S. Kashevarova, A. V. Rakhmanina *et al.*, JETP Lett. **63**, 818 (1996).
[5] C. S. Sundar, P. C. Sahu, V. S. Sactry *et al.*, Phys. Rev. B **53**, 8180 (1996).
[6] V. D. Blank, S. G. Buga, N. R. Serebryanaya *et al.*, Phys. Lett. A **200**, 149 (1996).
[7] L. Marques, J.-L. Hodeau, M. Nunez-Regueiro *et al.*, Phys. Rev. B **54**, R12633 (1996).
[8] V. Agafonov, V. A. Davydov, L. S. Kashevarova *et al.*, Chem. Phys. Lett. **267**, 193 (1997).
[9] A. Boultif and D. Louer, J. Appl. Crystallogr. **24**, 987 (1991).
[10] P. W. Stephens, G. Bortel, G. Faigel *et al.*, Nature (London) **370**, 636 (1994).
[11] A. V. Dzyabchenko, V. K. Bel'skiĭ, and P. M. Zorkiĭ, Kristallografiya **24**, 221 (1979) [Sov. Phys. Crystallogr. **24**, 127 (1979)].
[12] G. B. Adams, J. B. Page, O. F. Sankey *et al.*, Phys. Rev. B **50**, 17471 (1994).
[13] D. Porezag, M. R. Pederson, T. Franenheim *et al.*, Phys. Rev. B **52**, 14963 (1995).
[14] O. Chanvet, O. Oszlanyi, L. Forro *et al.*, Phys. Rev. Lett. **72**, 2721 (1994).
[15] H. A. Ludwig, W. H. Fietz, F. W. Hornung *et al.*, Z. Phys. B **96**, 179 (1994).
[16] M. Hanfland, H. Beister, and K. Syassen, Phys. Rev. B **39**, 12598 (1989).
[17] I. V. Aleksandrov, A. F. Goncharov, A. N. Zisman *et al.*, Zh. Éksp. Teor. Fiz. **93**, 680 (1987) [Sov. Phys. JETP **66**, 384 (1987)].

Translated by M. E. Alferieff

Anomalous behavior of textures in a magnetic field

A. M. Satanin
N. I. Lobachevski Nizhegorod State University, 603600 Nizhniĭ Novgorod, Russia

V. V. Skuzovatkin
Institute of Microstructure Physics, Russian Academy of Sciences, 603600 Nizhniĭ Novgorod, Russia

(Submitted 24 March 1997; resubmitted 19 June 1997)
Pis'ma Zh. Éksp. Teor. Fiz. **66**, No. 2, 115–119 (25 July 1997)

It is shown that a qualitatively new type of transition to a nonlinear phase is possible in two-dimensional two-phase textures in a magnetic field. The anomalous growth of the effective response (higher-order correlation functions of the current) near the critical magnetic field is studied. The dependence of the critical magnetic field on the angles of microinclusions is calculated. © *1997 American Institute of Physics.* [S0021-3640(97)01010-4]

PACS numbers: 68.55.Jk

Recent investigations of nonlinear and noise characteristics[1–3] have established a relation between these phenomena and the microgeometry of composite media and textures. It is well known that the effective characteristics of disordered materials, such as the electric or thermal conductivity, are insensitive to the microstructure of the material, since they are expressed in terms of the quadratic correlation functions of the fields and currents. The effective characteristics determined by the higher-order correlation functions may be anomalously sensitive to the microstructure of the medium. For example, the nonlinear resistance, the $1/f$-noise factor, and the amplitude of the third harmonic can be expressed in terms of the fourth moment of the electric field or current.[1,2,4,5] In Ref. 2, it was found that the higher-order moments can diverge because the fields diverge near the geometric singularities of microinclusions. In Ref. 3, it was noted that divergences are also possible in media with a finite ratio of the conductivity of microinclusions of composites. The anomalous properties of the higher-order moments make it possible to judge the microstructure of a medium on the basis of some effective characteristics of the medium. To establish the dependence of the response functions on the microstructure, it is necessary to investigate a representative sample of specimens containing nonuniformities whose microstructure is different and known in advance.

We show in the present letter that for a prescribed geometric structure of nonuniformities the divergences of the higher-order correlation functions of the electric fields and currents depend on the external magnetic field. The critical magnetic field in which there exists an anomalous fourth-order moment of the current corresponds for a given material to a transition from a classically weak-field regime to a classically strong-field regime. This property makes it possible to investigate the structure of micrononuniformities of specimens according to the macroscopic response and to realize a reversible transition to a nonlinear regime by varying the magnetic field.

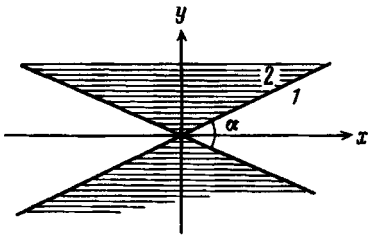

FIG. 1. Geometry of the micrononuniformity under study.

We shall be interested in the effective characteristics of a two-dimensional two-phase medium. The distribution of fields and currents is described by the equations

$$\mathbf{j}+\vec{\beta}[\mathbf{j}\times\mathbf{N}]=\sigma\mathbf{e},$$

$$\nabla\cdot\mathbf{j}=0, \quad \nabla\times\mathbf{e}=0, \tag{1}$$

where the conductivity σ and the Hall parameter assume the values σ_1, β_1, and σ_2, β_2 in the first and second phases, respectively. The magnetic field $\mathbf{B}=\mathbf{N}|\mathbf{B}|$ is directed perpendicular to the plane of the film. We shall confine our attention to the characteristics of the medium that can be expressed in terms of the correlation functions $\langle\mathbf{j}^4\rangle$ and $\langle\mathbf{e}^4\rangle$, where $\langle\ldots\rangle$ denotes averaging over the area of the film. As is well known,[4] the effective nonlinear resistance k_e in an isotropic medium is determined (to a first approximation in the nonlinearity) by the correlation function $k_e=\langle k\mathbf{j}^4\rangle/\langle\mathbf{j}\rangle^4$, where k is the local nonlinear resistance of the components. The amplitude of the third harmonic can likewise be expressed in terms of the correlation function $\langle k\mathbf{j}^4\rangle$.[1,5] A similar relation also holds for the effective $1/f$-noise factor.[1,2] It is easy to show that in a magnetic field these relations all hold for the dissipative characteristics measured in the Hall emf regime. For this reason, we shall study the dependence of the correlation function $\langle\mathbf{j}^4\rangle$ on the magnetic field and on the parameters of the system.

It is clear from physical considerations that all anomalies are most pronounced near a percolation transition, when the concentrations of the phases are approximately the same. As noted in Refs. 2, 3, and 6, the regions near microinclusions possessing sharp corners make the main contribution to the correlation function under study. In this case the simplest geometric objects can be distinguished from the entire system and their role in the formation of the response can be determined. In the case of periodic two-phase lattices, the main contribution to the correlation function $\langle\mathbf{j}^4\rangle$ appears near the corners made by alternate sectors with different conductivity.[6] In the present letter we shall examine some texture classes that are topologically close to those studied in Ref. 6. For example, the results presented below are applicable for a Poisson coating, when the plane is divided into cells by a random collection of straight lines (determined by a Poisson random process).[7] A general feature of the class of structures studied here is the presence of alternate sectors with different conductivity.

As shown in Ref. 6, in the absence of a magnetic field the most singular behavior of the fields occurs near points where four phases, formed by the intersection of two straight lines, are in contact (see Fig. 1). To find the current distribution in such a structure it is

necessary to solve Eq. (1) with the boundary conditions

$$(\mathbf{j}\cdot\mathbf{n})_1=(\mathbf{j}\cdot\mathbf{n})_2,$$
$$\left\{\frac{1}{\sigma}(\mathbf{j}+\vec{\beta}[\mathbf{j}\times\mathbf{N}])\cdot\mathbf{t}\right\}_1=\left\{\frac{1}{\sigma}(\mathbf{j}+\vec{\beta}[\mathbf{j}\times\mathbf{N}])\cdot\mathbf{t}\right\}_2, \tag{2}$$

where **n** and **t** are the normal and tangent vectors with respect to the interface separating the media. The current components can be represented in the polar coordinates (r,θ) in the form

$$j_r=\lambda r^{\lambda-1}f(\theta),\quad j_\theta=r^{\lambda-1}f'(\theta), \tag{3}$$

where the function f satisfies the equation $j''+\lambda^2 f=0$. On the basis of symmetry considerations (symmetry under inversion), it is sufficient to give the function f in two neighboring regions in the form

$$f_1(\theta)=a_1\cos\lambda\theta+b_1\sin\lambda\theta,$$
$$f_2(\theta)=a_2\sin\lambda(\pi/2-\theta)+b_2\cos\lambda(\pi/2-\theta), \tag{4}$$

since $f_3(\theta)=-f_1(\theta+\pi)$ and $f_4(\theta)=-f_2(\theta+\pi)$. It follows from the boundary conditions that this solution occurs for λ determined by the expression

$$\cot(\lambda\alpha/2)\cot(\lambda(\pi-\alpha)/2)=\frac{1+h^2+b^2+\sqrt{(1+h^2+b^2)^2-4h^2}}{2h}, \tag{5}$$

where $b=h\beta_1-\beta_2$ and $h=\sigma_2/\sigma_1$. For $h<1$, the solution obtained corresponds to a situation when the current ''leaks'' through narrow constrictions formed by sectors with low conductivity σ_2. As one can see from Eqs. (3), the squared current in each sector depends on distance as

$$j^2(r)\sim r^{-4\gamma},\quad \gamma=(1-\lambda)/2,\quad 0\leqslant\gamma\leqslant 1/2. \tag{6}$$

The quantity γ is a function of the prescribed structural parameters h and α. It is important to note that for $\sigma_2/\sigma_1\neq\beta_2/\beta_1$ the parameter γ depends on the magnetic field. The qualitative explanation of this behavior is as follows. Since the Laplace equation is homogeneous and there are no spatial scales, the current is a power-law function of distance. The exponent γ is determined by the charge density induced on the phase boundaries. The charge density in turn depends on the Hall component of the electric field and thereby on the intensity of the magnetic field. There also exists another particular solution which has no singularities near a distinguished angle. The contribution of this solution to the correlation function $\langle\mathbf{j}^4\rangle$ is small compared with the contribution from Eq. (6) and therefore can be neglected. We shall estimate, on the basis of the particular solution obtained, the contribution of micrononuniformities of the type under consideration to the correlation function $\langle\mathbf{j}^4\rangle$. For this, we integrate $\mathbf{j}^4$ near the special corners over a region with characteristic distance L (L is the characteristic distance between the special corners). This average can be written as

$$\langle\mathbf{j}^4\rangle\sim\int_0^L\frac{dr}{r^{8\gamma-1}}. \tag{7}$$

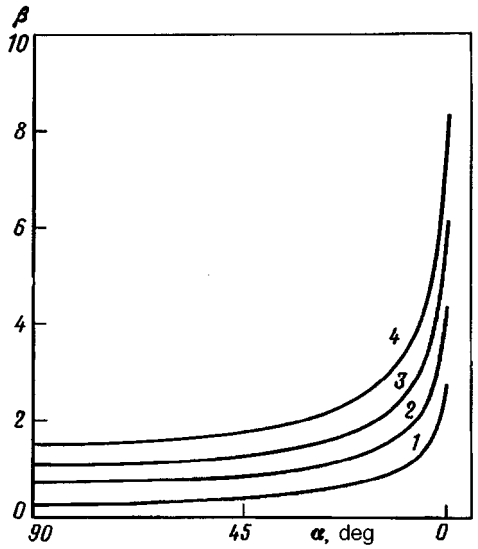

FIG. 2. Critical Hall parameter β_c as a function of angle for different values of the parameter h (curve *1* — $h=0.2$; curve *2* — $h=0.4$; curve *3* — $h=0.6$; curve *4* — $h=0.8$).

Hence the integral diverges if $\gamma \geqslant 1/4$. The critical value $\gamma_c = 1/4$ corresponds to the critical magnetic field B_c determined by the expression

$$B_c = \sqrt{\frac{(1+C^2)h-(1+h^2)C}{C(h\nu_1-\nu_2)^2}}, \tag{8}$$

where $C=\cot(\alpha/4)\cot((\pi-\alpha)/4)$, $\nu_1=\beta_1/B$, and $\nu_2=\beta_2/B$(as is well known, for one group of carriers the ratio $\nu=\beta/B$ is virtually independent of the magnetic field). It is important to note that for prescribed parameters of a micrononuniformity there exists a critical magnetic field for which the effective characteristics of the system expressed in terms of $\langle \mathbf{j}^4 \rangle$ become anomalously large. It is easy to show that for $\beta_1 \sim \beta_2$, $h \sim 1$, and $\alpha \sim \pi/2$ the critical Hall parameter $\beta_c = \omega_c \tau \sim 1$. Figure 2 displays β_c as a function of angle for different values of the parameter h. As one can see in Fig. 2, in a wide range of angles near $\pi/2$ the critical Hall parameter β_c is virtually angle-independent.

The qualitative arguments presented above can be confirmed by an exact calculation of the correlation function $\langle \mathbf{j}^4 \rangle$ for a square lattice with a checkerboard structure. The exact current distribution in the cells in a magnetic field is obtained in Ref. 8. In our case the expression for the correlation function depends on the direction of the external current. The character of the divergence of the correlation function, however, does not depend on the direction of the external current. For this reason, we shall choose it in a manner so that singularities of the type (6) remain in the local current only along the common diagonals in each cell.[8] The calculation of the correlation function $\langle \mathbf{j}^4 \rangle$ using the expression for the current from Eq. (8) gives

$$\langle \mathbf{j}^4 \rangle = A/(B_c - B), \quad B_c - B \ll B_c, \tag{9}$$

where A is a constant that depends on the external current and the ratio of the cell conductivities, and the critical field B_c is determined by the relation

$$B_c = \sqrt{8h-(1+h)^2}/|h\nu_1 - \nu_2|. \tag{10}$$

It is easy to see that expression (8) is identical to Eq. (10) with $\alpha = \pi/2$.

It is interesting to compare the magnetic field dependence of the correlation functions $\langle \mathbf{j}^2 \rangle$ and $\langle \mathbf{j}^4 \rangle$ for structures which possess the same type of micrononuniformity. As was shown in Refs. 8–10, the correlation function $\langle \mathbf{j}^2 \rangle$ can be calculated for a random equal-composition system[9,10] and a periodic lattice.[8] It follows from the exact solutions that for these systems the results are identical. In classically weak fields $\omega_c \tau \ll 1$ the correlation function $\langle \mathbf{j}^2 \rangle$ has a quadratic correction in the field, and for $\omega_c \tau \gg 1$ the correlation function increases as $\sim B$. This investigation shows that the behavior of the correlation function $\langle \mathbf{j}^4 \rangle$ is qualitatively different from that of $\langle \mathbf{j}^2 \rangle$.

In summary, a qualitatively new behavior of the effective characteristics of a system which are expressed in terms of the correlation function $\langle \mathbf{j}^4 \rangle$ (nonlinear resistance, noise factor, and amplitude of the third harmonic) has been predicted. It has been shown that as $B \to B_c$ the indicated characteristics grow anomalously. For $B > B_c$ the system transforms reversibly into a strongly nonlinear current-flow regime. Evidently, the predicted anomaly is most easily observed in the generation of a third harmonic. As shown above, the anomalous regime is possible when $\omega_c \tau \geqslant 1$, which is identical to the condition for observing cyclotron resonance for the corresponding specimens.

After writing this letter we learned that Dykhne obtained similar results earlier.[11] In Ref. 11 it was shown that the higher-order correlation functions of the current in two-dimensional structures diverge on account of small neighborhoods of corners where sectors with different conductivity meet.

One of us (A. M. S.) thanks Dr. D. Jeulin for very helpful discussions of some questions discussed in this letter.

This work was supported by State Committee of the Russian Federation on Higher Education (Grant No. 95-0-7.4-173) and the Russian Fund for Fundamental Research (Grant No. 97-02-16923a).

[1] M. A. Dubson, Y. C. Hui, M. B. Weissman, and J. C. Garland, Phys. Rev. B **39**, 6807 (1989).
[2] D. J. Bergman, Phys. Rev. B **39**, 4598 (1989).
[3] A. M. Dykhne, V. V. Zosimov, and S. A. Rybak, Dokl. Akad. Nauk Ross. Akad. Nauk **345,** 467 (1995).
[4] D. Stroud and P. M. Hui, Phys. Rev. B **37**, 8719 (1988).
[5] A. A. Snarskiĭ, Pis'ma Zh. Tekh. Fiz. **21**(1), 3 (1995) [Tech. Phys. Lett. **21**, 1 (1995)].
[6] A. M. Satanin, V. V. Skuzovatkin, and S. V. Khor'kov, JETP Lett. **64**, 538 (1996).
[7] J. M. Ziman, *Models of Disorder: The Theoretical Physics of Homogeneously Disordered Systems*, Cambridge University Press, New York, 1979 [Russian translation, Mir, Moscow, 1982].
[8] Yu. P. Emets, *Electrical Characteristics of Composite Materials with a Regular Structure* [in Russian], Naukova Dumka, Kiev, 1986.
[9] A. M. Dykhne, Zh. Éksp. Teor. Fiz. **59,** 641 (1970) [Sov. Phys. JETP **32**, 348 (1971)].
[10] B. Balagurov, Fiz. Tverd. Tela (Leningrad) **20,** 3332 (1978) [Sov. Phys. Solid State **20**, 1922 (1978)].
[11] A. M. Dykhne, Phystech. J. **2,** 3 (1996).

Translated by M. E. Alferieff

ERRATA

Erratum: Instability of the two-dimensional metallic phase to a parallel magnetic field [JETP Lett. 65, No. 12, 932–937 (25 June 1997)]

V. M. Pudalov
Institut für Halbleiterphysik, Johannes Kepler Universität Linz, A-4040 Linz, Austria; Institute for High Pressure Physics, 142092 Troitsk, Moscow Region, Russia

G. Brunthaler, A. Prinz, and G. Bauer
Institut für Halbleiterphysik, Johannes Kepler Universität Linz, A-4040 Linz, Austria

Pis'ma Zh. Éksp. Teor. Fiz. **66**, No. 2, 120 (25 July 1997)

[S0021-3640(97)01114-6]

PACS numbers: 73.40.Hm, 71.30.+h, 99.10.+g

The list of references should be modified to reflect the following corrections:

[7]B. L. Altshuler and A. G. Aronov, in *Electron–Electron Interaction in Disordered Systems*, edited by A. L. Efros and M. Pollak, North-Holland, Amsterdam, 1985.

[8]H. Fukuyama, *ibid.*, p. 155.

[9]For recent results see *Proceedings of the International Conference on Electron Localization and Quantum Transport in Solids*, Jaszowiec, Poland, edited by T. Dietl, Institute of Physics, Polish Academy of Sciences, Warsaw, Poland, 1996.

[10]G. Brunthaler, T. Dietl, M. Sawicki *et al.*, Semicond. Sci. Technol. **11**, 1624 (1996).

[11]D. Simonian, S. V. Kravchenko, and M. P. Sarachik, cond-mat/9704071.

[12]V. M. Pudalov, *op. cit.* 9, p. 34.

[13]D. J. Bishop, R. J. Dynes, and D. C. Tsui, Phys. Rev. B **26**, 773 (1982).

[14]A. E. Voiskovsky and V. M.Pudalov, JETP Lett. **62**, 947 (1995).

[15]A. J. Dahm, F. W. Van Keuls, H. Mathur, and H. W. Jiang, *op. cit.* 9, p. 33.

[16]A. Efros, F. G. Pikus, and E. V. Tsiper, *op. cit.* 9, p. 10.

The contribution of the $(t(\tau)+N)$ component to the α-particle wave function from data on the reactions $p(\alpha,pp)t$ and $p(\alpha,pn)\tau$ at incident α-particle momentum 5 GeV/c

M. V. Chadeyeva, V. E. Grechko, V. V. Solov'ev, and V. F. Turov
Institute of Theoretical and Experimental Physics, 117259 Moscow, Russia

(Submitted 23 May 1997)
Pis'ma Zh. Éksp. Teor. Fiz. **66**, No. 2, 69–74 (25 July 1997)

The 2-meter liquid-hydrogen bubble chamber is exposed to a separated beam of α particles from the ITEP synchrotron. The momentum of the incident ^{4}He nuclei, averaged over the fiducial volume of the chamber, is 5 GeV/c (the kinetic energy of initial protons in the nucleus rest frame is $T_p=$ 620 MeV). The spectral functions of decays $\alpha\to tp$ and $\alpha\to\tau n$ are extracted in the 4π geometry (the latter is extracted for the first time) from the exclusive reactions $\alpha p\to tpp$ and $\alpha p\to\tau pn$ in the spectator momentum region $0<q<0.3$ GeV/c. The pole dominance criteria are carefully checked. Extrapolation of the nuclear vertex function to the pole gives a lower bound on the nuclear vertex constant. Our experimental data are compared with the results of other studies and with theoretical calculations. © *1997 American Institute of Physics.* [S0021-3640(97)00114-X]

PACS numbers: 25.55.Ci

The momentum distributions (spectral functions SFs) are among the most important characteristics of the ^{4}He nucleus. They are defined as the square of overlap integrals between the wave functions (WFs) of the nucleus and of the spectator nuclear fragments $(t(\tau),dN,3N)$.

We have previously[1] extracted the SFs for the virtual two-particle decays $\alpha\to t(\tau)N$ $(t\equiv{}^3\mathrm{H},\ \tau\equiv{}^3\mathrm{He})$ from the reactions

$$p(\alpha,pp)t, \tag{1}$$

$$p(\alpha,pn)\tau, \tag{2}$$

at an initial α-particle momentum 2.7 GeV/c in the spectator momentum region $0<q<0.16$ GeV/c (in this case due to the small phase space value the contribution of the diagram with three-nucleon nuclear exchange (Fig. 1b) is already significant at $q\sim$ 0.2 GeV/c).

Particular attention was paid to the accurate selection of quasifree pN scattering (QFS) events, which correspond to the diagram of Fig. 1a. The criteria of pole dominance

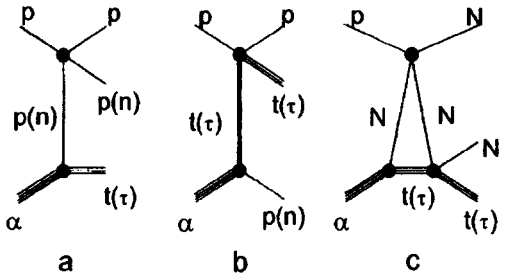

FIG. 1. The simplest diagrams for the reactions $p\alpha \to t(\tau)pN$.

described in Ref. 2 were checked — in particular, the Treiman–Yang criterion, which is very sensitive to the contribution of mechanisms other than the pole mechanism (especially, to the final-state interaction (FSI) mechanism of Fig. 1c).

In this paper we present preliminary data (70% of the expected statistics) on SFs from the reactions (1) and (2) at an initial α-particle momentum of 5 GeV/c. There are two main goals here: a) verification that the SFs are independent of the initial momentum of incident α particle, which would confirm the validity of the SF extraction, and b) expansion of the phase space so that the contribution of the diagram of Fig. 1b can be neglected up to momenta $q \sim 0.3$ GeV/c.

The experimental data were obtained on the 2-meter liquid-hydrogen bubble chamber of ITEP. This chamber was exposed to a separated beam of α particles; their momentum, averaged over the fiducial volume, was 5 GeV/c (with this experimental technique the nuclear fragments can be fast particles and thus be measured with high accuracy). We selected 1445 events of the reaction $\alpha p \to tpp$ and 1824 events of the reaction $\alpha p \to \tau pn$. The method used to extract the spectral functions from the experimental data was described in detail in our previous papers.[3,4]

As follows from analysis of the matrix element of the QFS diagram of Fig. 1a, there is a simple relation between spectral functions ρ_{tN} of two-particle decays $\alpha \to t(\tau)N$ and the differential cross sections of reactions (1) and (2) $d\sigma/dq^2$:

$$\rho_{tN}(q) = \frac{8m\pi^2\lambda(s,m^2,m_\alpha^2)}{m_\alpha^2\Phi(t_1)}\frac{d\sigma}{dq^2}. \tag{3}$$

Here q is three-particle nuclear momentum in the rest frame of the ^{4}He nucleus, m is the mass of the nucleon, m_α is the mass of ^{4}He nucleus, $\lambda(x,y,z) = (x+y+z)^2 - xyz$, s is the square of the total invariant mass, t_1 is the square of the 4-momentum transferred from the ^{4}He nucleus to the three-nucleon nucleus, and $\Phi(t_1)$ is defined as follows:

$$\Phi(t_1) = \int_{\max\{s_-(t_1),4m^2\}}^{s_+(t_1)} ds_1 \sigma_{\rm el}^{(pN)}(s_1,t_1)\lambda^{1/2}(s_1,m^2,m^2). \tag{4}$$

Here s_+ and s_- are calculated using the formulas given in Ref. 3 with the corresponding mass substitution, s_1 is the square of the total mass of the pN system, $\sigma_{\rm el}^{(pN)}$ is given by the following formula:

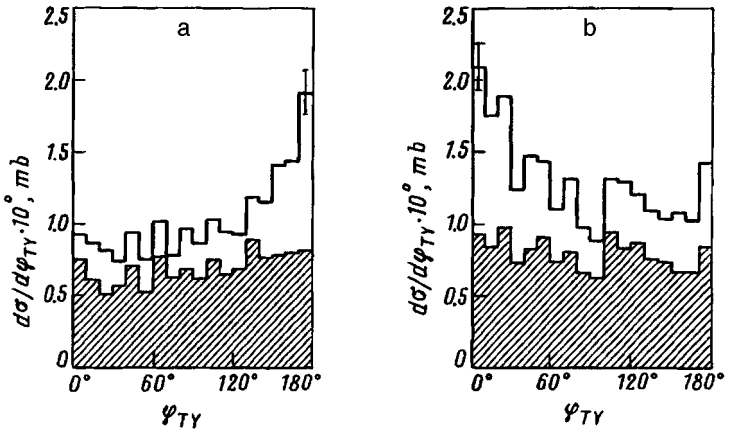

FIG. 2. Treiman–Yang angle distributions for the reactions: a — $\alpha p \to tpp$ and b — $\alpha p \to \tau pn$. Clear histograms correspond to the total number of events, shaded histograms correspond to the events remaining after two constraints are imposed (see text above).

$$\sigma_{\rm el}^{(pN)}(s_1,t_1) = 2\pi(1-I_z^{pN}/2)\int_{-c_1}^{c_2} \frac{d\sigma^{(pN)}(s_1,t_1)}{d\Omega^*} d\cos\theta^*. \tag{5}$$

Here $I_z^{(pN)}$ is the third isospin projection of the pN system, $d\sigma^{(pN)}(s_1,t_1)/d\Omega^*$ is the off-shell cross section of elastic pN scattering, θ^* is the scattering angle between the initial and outgoing protons in the center-of-mass system of the pN pair. The choice of the limits of integration c_1 and c_2 will be discussed below.

Two constraints were imposed to select the events corresponding to the QFS diagram (Fig. 1a): I) $q<0.3$ GeV/c and II) $-c_1<\cos\theta^*<c_2$. One has $c_1=c_2=0.7$ for reaction (1) and $c_1=c_2=0.8$ for reaction (2). After these constraints we imposed, 968 events of reaction (1) and 1106 events of reaction (2) remained.

The first constraint is needed to exclude the contribution of the diagram of Fig. 1b (with three-nucleon nuclear exchange). This contribution is shown by our calculations to be negligible at an initial energy $T_p=$ 620 MeV and $q<0.3$ GeV/c (Monte Carlo calculations were performed; the elastic cross sections for pN, pt, and $p\tau$ were taken on the mass shell in the entire kinematically allowed region, the Glauber–Sitenko model was used for the calculation of the pt and $p\tau$ elastic cross sections, and the pN amplitudes were taken from phase space analysis; the SFs ρ_{tN} were taken from the theoretical calculations[5,6]).

The second constraint makes it possible to exclude significantly the phase space region in which the FSI is substantial.[3,4,7]

The following results are obtained after imposing the constraints I and II to the experimental data on the reactions (1) and (2): *1*) as is seen from Fig. 2, the Treiman–Yang angle distributions are practically isotropic, i.e., the necessary pole dominance criterion is satisfied[2] ($\phi_{\rm TY}$ is the angle between the plane formed by the momenta of the α particle and the t (or τ) nucleus and plane formed by the momenta of the outgoing

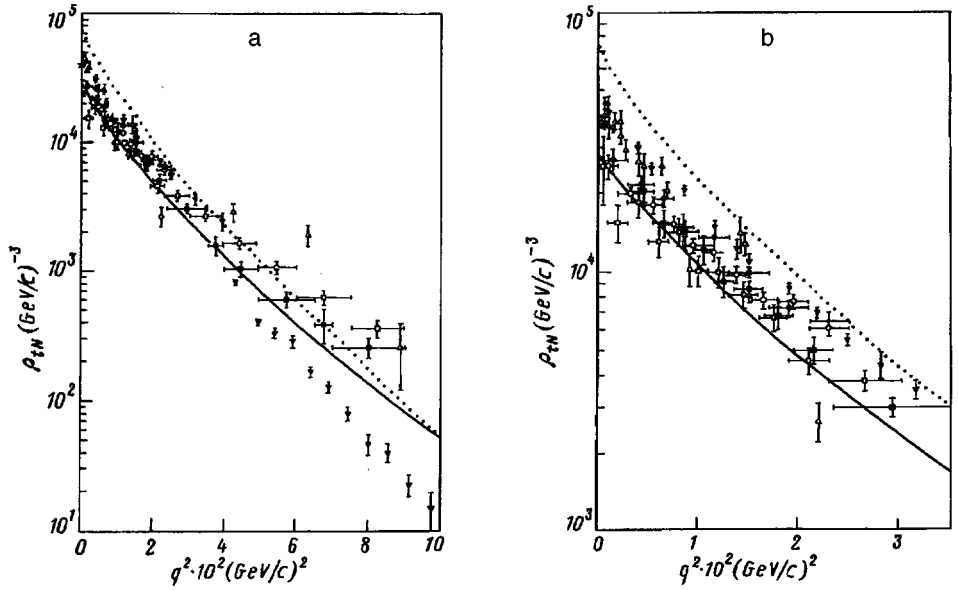

FIG. 3. a — spectral functions $\rho_{tN}(q)$: ○ and ● — our data (averaged over the corresponding interval of q^2) at $T_p = 220$ MeV on the reactions $p(\alpha,pn)\tau$ and $p(\alpha\ ,\ pp)t$, respectively,[1] ■ and ■ — our data at $T_p = 620$ MeV for the same reactions, respectively (see also Table I), ▽ — NIKHEF data[14] on the reaction $\alpha(e,e'p)t$ at $T_e = 426$ MeV, △ — data of Ref. 15 for the reaction $\alpha(p,pp)t$ at $T_p = 590$ MeV. The dotted and solid lines are the theoretical calculations from Refs. 5 and 6, respectively; b — the scaled part of (a) in the region of small q.

nucleons, all momenta being taken in the rest frame of the initial proton); *2*) the nuclear vertex function (NVF) will be shown below to be linear in q^2 in the region of small q; *3*) the average momentum transfer from the initial proton to the fastest outgoing nucleon is ~ 0.8 GeV/c, which is sufficiently greater than the inverse nuclear radius (~ 0.12 GeV/c); *4*) the fraction of events for which the relative kinetic energy of the $Nt(\tau)$ system is less than 80 MeV (when the FSI effect is expected to be critical) really does not exceed 25%; *5*) the fraction of events with noncoplanarity angle greater than 6° does not exceed 10%; *6*) the stronger constraint ($|\cos\theta^*| < 0.6$) causes no changes in ρ_{tN} within the error, while giving significant improvement of the above characteristics *3–5* of FSI event suppression; *7*) the SFs are independent of the initial energy within the error (see Fig. 3).

Thus, the results *1–7* show the validity of the QFS event selection.

To obtain SFs from data on the reactions (1) and (2) the elastic cross sections of pN scattering were parametrized on the mass shell in the entire kinematically allowed region using phase shift analysis.[8,9] The influence of off-shell effects in the framework of Mongan model[10] was estimated in our previous work,[1] where we extracted the SFs from reactions (1) and (2) at an α-particle momentum of 2.7 GeV/c (i.e., at a kinetic energy of 220 MeV, which is nearly the limit of applicability of the model). It turns out that the off-shell effects can increase the SFs by 10% in the region $q < 85$ MeV/c and on average by 30% in the region $85 < q < 160$ MeV/c.

It should be mentioned that in the case of two-particle decay of the α particle, $\alpha \to t(\tau)N$, the off-shell effects, which depend on the difference between the binding energies $\epsilon_\alpha - \epsilon_{t(\tau)} \approx 20$ MeV, are much greater than for the two-particle decay of three-nucleon nuclei $t(\tau) \to Nd$, where $\epsilon_t(\tau) - \epsilon_d \approx 6$ MeV.[3,7]

Let us define the nuclear vertex function for zero orbital angular momentum l of relative motion of the nucleon and three-nucleon nucleus ($l=0$ unambiguously for $\alpha \to t(\tau)N$) as follows:

$$W(q) = \frac{2}{3m}(q^2+\kappa^2)\sqrt{\rho_{tN}(q)}, \quad \kappa^2 = \frac{3m}{2}(\epsilon_\alpha - \epsilon_{t(\tau)}). \tag{6}$$

The experimental values of the NVF $W(q)$ extracted from the full set of our data on reactions (1) and (2) at initial momenta of 2.7 and 5 GeV/c are well fitted by the straight line $W(q) = a_0 + a_1 q^2$ in the region $q < 0.1$ GeV/c (the number of terms in the series was determined by the Fisher criterion). The following parameter values were obtained: $a_0 = (3.51 \pm 0.05)$ $(\text{GeV}/c)^{-1/2}$ and $a_1 = (-44 \pm 2)$ $(\text{GeV}/c)^{-5/2}$ with $\chi^2/DF = 0.86$.

Following our method[3] for investigating the Coulomb corrections for the decay $\tau \to pd$, we found that the Coulomb screening for the decay $\alpha \to p\tau$ was less than a few percent.

As was mentioned above, the linear behavior of the NVF with respect to q^2 in the region of small q verifies the validity of event selection in the phase space region where the pole diagram of Fig. 1a dominates (see also Ref. 11).

By extrapolating the NVF $W(q)$ to the pole at $q^2 = -\kappa^2$ the value of the nuclear vertex constant NVC (notation of Ref. 12) was found to be $G^2_{\alpha tN} = (4.5 \pm 0.1)$ fm. A wide spread of NVC values obtained by other phenomenological methods was given in Ref. 12 (from 7 fm up to 18 fm). Due to the well-known statement that the NVC is essentially nonlinear in the unphysical region, the extracted value must be regarded as a lower bound on the real NVC. It should be noted that in the compound-quark bag model $G^2_{\alpha tN} = 5.7$ fm.[13]

Our results on $\rho_{tN}(q)$ are shown both in Table I and in Fig. 3 (where Fig. 3b is a scaled part of Fig. 3a in the region of small q). Figure 3 also includes our earlier data from Ref. 1, the results of experimental works[14,15] as well as the theoretical calculations for NN potentials RSCV_8 from Ref. 5 and Argonne v18 from Ref. 6 (the three-particle forces were taken into account in the framework of the Urbana IX potential). The data from Ref. 16 (not shown) are very close to those of Ref. 15 (due to the difference in normalization procedure, the data of Refs. 5 and 6 and 14–16 must be multiplied by the constant value $(2\pi)^3$ to compare with our data). As is seen from Fig. 3, the spectral functions $\rho_{tN}(q)$ from reactions (1) and (2) at initial α-particle momenta of 2.7 and 5 GeV/c are in good agreement within experimental error.

Our data lie systematically lower than the experimental date of Refs. 14–16, the discrepancy reaching 50% in the region $q < 0.05$ GeV/c. In contrast, our data lie higher than the NIKHEF results[14] in the region $0.2 < q < 0.3$ GeV/c, the discrepancy in the tail being nearly an order of magnitude. As to the theoretical calculations, the results of Schiavilla and Wiringa[6] are seen from Fig. 3 to be in better agreement with our experimental data, especially at small q. It should be mentioned that the theoretical calculations

TABLE I. Spectral function $\rho_{tN}(q)$ from the reactions $p(\alpha,pn)\tau$ and $p(\alpha,pp)t$ at $T_p=$ 620 MeV.

Range of averaging over $q^2\times10^3$(GeV/c)^2	$\rho_{tN}(q)\times10^{-4}$(GeV/$c$)$^{-3}$ from the reaction $p(\alpha,pn)\tau$	Range of averaging over $q^2\times10^3$(GeV/c)^2	$\rho_{tN}(q)\times10^{-4}$(GeV/$c$)$^{-3}$ from the reaction $p(\alpha,pp)t$
0−1	2.56±0.76	3.5−5.5	2.03±0.24
1−3	1.54±0.25	5.5−7.5	1.53±0.19
3−5	1.84±0.23	7.5−9.5	1.47±0.18
5−7	1.30±0.17	9.5−11.5	1.21±0.15
7−9	1.41±0.17	11.5−13.5	0.91±0.13
9−11	1.00±0.13	13.5−16.5	0.85±0.10
11−13	0.99±0.13	16.5−19.5	0.67±0.08
13−16	0.81±0.09	19.5−23.5	0.50±0.06
16−19	0.66±0.08	23.5−35	0.30±0.02
19−23	0.45±0.05	35−39.5	0.15±0.02
23−30	0.38±0.03	39.5−49.5	0.10±0.01
30−39	0.26±0.02	49.5−65	0.06±0.01
39−49	0.16±0.02	65−70	0.04±0.01
49−60	0.10±0.01	70−90	0.02±0.005
60−75	0.06±0.01		
75−90	0.03±0.01		

from Refs. 5 and 6 are in sharp contradiction with each other at small q, clearly showing the strong dependence of the spectral functions on the choice of NN potential.

Including in the analysis all our experimental data on reactions (1) and (2) at two different initial momentum values, we approximated the function $\rho_{tN}(q)$ as follows: $A_1\exp(-b_1q^2)+A_2\exp(-b_2q^2)$; the following parameter values were obtained at $\chi^2/DF=1.45$: $A_1=(2.5\pm0.2)\times10^4$ (GeV/c)$^{-3}$, $b_1=74\pm2$ (GeV/c)$^{-2}$, $A_2=(6.4\pm3.4)\times10^2$ (GeV/c)$^{-3}$, $b_2=12\pm4$ (GeV/c)$^{-2}$.

Finally, after integration of this function with the given above parameters values in the region $0<q<0.3$ GeV/c the contribution of the $(t(\tau)+N)$ component

$$N_{tN}=\frac{1}{(2\pi)^3}\int\rho_{tN}d^3q$$

to the ^{4}He nucleus was found to be 1.05. As follows from our recent work,[17] the contribution of the $(d+d)$ component to the wave function of the ^{4}He nucleus,

$$N_{dd}=\frac{1}{(2\pi)^3}\int\rho_{dd}d^3q,$$

in the same region of q equals 0.54. These results are very important for checking the sum rule for the total spectral function, which includes the contributions of two-, three- and four-body virtual decays of the ^{4}He nucleus.

The authors are very grateful to our colleagues S. M. Zombkovsky, A. V. Blinov, and Yu. V. Korolev for their valuable assistance in this investigation. We also would like

to thank R. Schiavilla for the given results of his recent theoretical calculations. This work has been partly supported by the Fund for Fundamental Nuclear Physics.

[1] S. K. Abdullin, A. V. Blinov, I. A. Vanyushin *et al.*, Phys. At. Nucl. **56**, 670 (1993).
[2] V. M. Kolybasov, G. A. Leksin, and I. S. Shapiro, Usp. Fiz. Nauk **113**, 299 (1974) [Sov. Phys. Usp. **17**, 381 (1974)].
[3] A. V. Blinov, I. A. Vanyushin, V. E. Grechko *et al.*, J. Phys. G.: Nucl. Phys. **11**, 623 (1985).
[4] A. V. Blinov, I. A. Vanyushin, V. E. Grechko *et al.*, Nucl. Phys. A **469**, 566 (1987).
[5] H. Morita, Y. Akaishi, and H. Tanaka, Prog. Theor. Phys. **79**, 863 (1988).
[6] R. Schiavilla and R. B. Wiringa, Private communication, 1995.
[7] A. V. Blinov, I. V. Chuvilo, V. V. Drobot *et al.*, Nucl. Phys. A **451**, 701 (1986).
[8] R. A. Arndt, L. D. Roper, R. A. Bryan *et al.*, Phys. Rev. D **28**, 97 (1983).
[9] R. Dubois, D. Axen, R. Keeler *et al.*, Nucl. Phys. A **377**, 554 (1982).
[10] T. R. Mongan, Phys. Rev. **178**, 1597 (1964).
[11] A. W. Stetz, Phys. Rev. C **21**, 1979 (1980).
[12] A. G. Baryshnikov, L. D. Blokhintsev, and I. M. Narodetskii, Nucl. Phys. A **272**, 327 (1976).
[13] A. G. Baryshnikov, L. D. Blokhintsev, I. M. Narodetskii, and D. A. Slavin, Yad. Fiz. **48**, 1273 (1988) [Sov. J. Nucl. Phys. **48**, 809 (1988)].
[14] J. F. J. van der Brandt, H. P. Blok, H. J. Bulten *et al.*, Phys. Rev. Lett. **66**, 409 (1991).
[15] C. F. Perdrisat, L. W. Swenson, P. G. Gugelot *et al.*, Phys. Rev. **187**, 1201 (1969).
[16] W. T. H. van Oers, B. T. Murdoch, B. K. S. Koene *et al.*, Phys. Rev. C **25**, 390 (1982).
[17] V. E. Grechko, S. M. Zombkovskii, Yu. V. Korolev *et al.*, Phys. Lett. B **343**, 41 (1995).

Published in English in the original Russian journal. Edited by Steve Torstveit.

How can we study the halo momentum distribution in exotic nuclei?

G. D. Alkhazov[a)]
St. Petersburg Nuclear Physics Institute, 188350 Gatchina, Leningrad District, Russia

(Submitted 30 May 1997)
Pis'ma Zh. Éksp. Teor. Fiz. **66**, No. 2, 75–80 (25 July 1997)

Conditions for applicability of the ''sudden'' approximation to the description of fragmentation of exotic nuclei are discussed. An experiment is proposed that may yield rather accurate information on the halo internal momentum distribution. © *1997 American Institute of Physics.* [S0021-3640(97)00214-4]

PACS numbers: 36.10.−k, 25.70.Mn

Since the discovery of exotic nuclei,[1] which have an unusual spatial structure with a normal-sized nuclear core and an extended nucleon halo, their properties have been studied extensively by different methods. Much valuable information on the nuclear structure of exotic nuclei has been obtained from the data on nuclear fragmentation. Nevertheless, the situation with the nucleon momentum distributions in these nuclei still remains uncertain. It turns out that the mechanism of the nuclear fragmentation reaction may significantly affect the momentum distributions obtained. Thus it is still not quite clear to what extent the measured distributions reflect the true internal ones.[2,3]

The idea of the nuclear fragmentation experiments is as follows. A beam of exotic nuclei intersects a fragmentation target. Due to interaction with the target, nuclear breakup (or the Coulomb dissociation) takes place. In the beginning of these studies it was supposed, with a reference to the ''sudden'' approximation, that the observed fragment momentum distributions were the true internal ones. The sudden approximation implies that the participants of the interaction are removed from the nucleus under study so quickly that the rest of the nuclear system may be supposed intact, its momentum being the same as it was before the interaction. In fragmentation reactions, however, the conditions for applicability of the sudden approximation are usually not fulfilled. Indeed, even when the experiment is performed at relatively high energy, so that the target crosses the nucleus rather rapidly (in the center-of-mass reference frame of the nucleus), the rescattering of the target on the nuclear components violates the applicability of this approximation. Moreover, the nuclear participants in the interaction with the target may not be removed from the nucleus fast enough. The sudden approximation fails for this reason as well.

Let us consider main mechanisms of intermediate-energy fragmentation of a one-neutron-halo exotic nucleus to a core and a neutron. We assume that the exotic nucleus consists of two well separated by-systems, a halo neutron and a core, so that its wave function may be represented as $\Psi_{f,i}=\varphi_{f,i}(\mathbf{r})\psi_c$, where $\varphi_{f,i}(\mathbf{r})$ describes the relative motion of the neutron and the core, and ψ_c describes the internal motion of the core

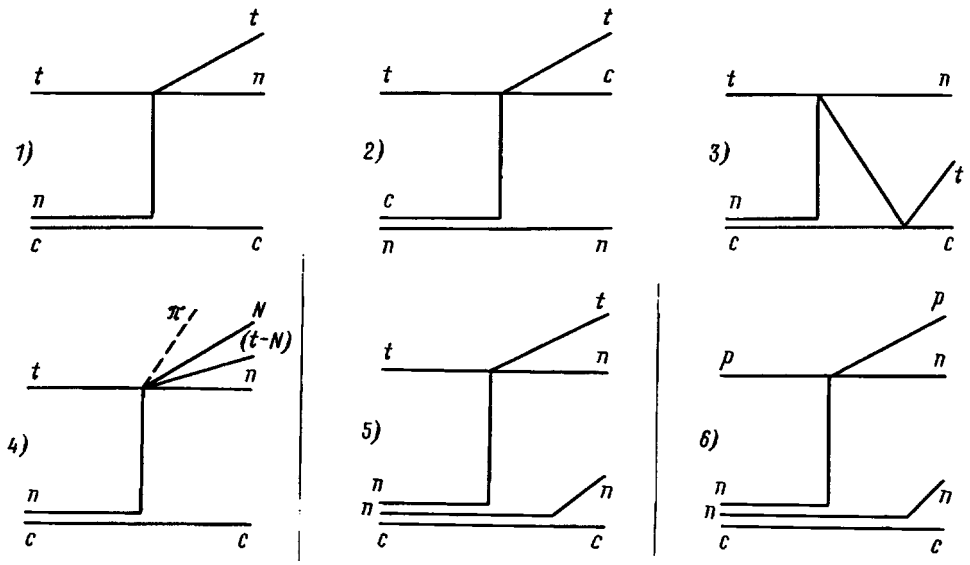

FIG. 1. Main diagrams for fragmentation of exotic nuclei (t — target; c — core; n — halo nucleon; N — target nucleon; p — proton; π — pion).

nucleons. Let **q** be the momentum transfer from the target to the exotic nucleus. Since the binding energy of the halo neutron is low, even small momentum transfers may induce fragmentation of the exotic nucleus, the target nucleus being left in the ground state. Thus, it is evident that the ''elastic'' breakup (the target nucleus being left in the ground state) is an important channel of exotic nucleus fragmentation. Describing the target interaction with the exotic nucleus as consecutive independent interactions of the target with the halo neutron and with the core, and using the Glauber–Sitenko theory, we obtain the well-known formula[4,5] for the amplitude of elastic breakup:

$$F_{fi}(\mathbf{q})=(ik/2\pi)\int \exp(i\mathbf{qb})\langle\varphi_f|\Gamma(\mathbf{b})|\varphi_i\rangle d^2b, \tag{1}$$

$$\Gamma(\mathbf{b})=\Gamma_{tn}(\mathbf{b}-\mathbf{s}_n)+\Gamma_{tc}(\mathbf{b}-\mathbf{s}_c)-\Gamma_{tn}(\mathbf{b}-\mathbf{s}_n)\Gamma_{tc}(\mathbf{b}-\mathbf{s}_c). \tag{2}$$

Here $\Gamma(\mathbf{b})$ is the profile function for the interaction between the target and the exotic nucleus; **b** is the relevant impact vector; k is the value of the wave vector of the projectile; $\Gamma_{tn}(\mathbf{b}-\mathbf{s}_n)$ and $\Gamma_{tc}(\mathbf{b}-\mathbf{s}_c)$ are the profile functions for the interactions between the target and the halo neutron, and between the target and the core of the exotic nucleus, respectively; $\mathbf{s}_n$ and $\mathbf{s}_c$ are the transverse coordinates of the neutron and the core.

The three terms in Eq. (2) are presented in Fig. 1 by the corresponding diagrams *1*, *2*, and *3*. Let us consider the first diagram, which corresponds to fragmentation due to ''elastic'' scattering of the halo neutron on the target. Due to its low binding energy, the halo neutron spends a significant part of its time beyond the range of the nuclear forces of the core. This allows us to suppose that in the breakup process the effect of the

final-state interaction between the knocked-off neutron and the core is not essential, so that the wave function $\varphi_f(\mathbf{r})$ may be taken as a plane wave. Then from Eq. (1) and from the first term of Eq. (2), it follows immediately that

$$d\sigma/d^3k_c = \sigma_{tn}\rho(\mathbf{k}_c), \quad d\sigma/d^3k_n = \int (d\sigma_{tn}(\mathbf{q})/d^2q)\rho(\mathbf{k}_n - \mathbf{q})d^2q. \tag{3}$$

Here $d\sigma/d^3k_n$ and $d\sigma/d^3k_c$ are the breakup cross section distributions over experimentally observed neutron and core-fragment momenta (in the CM system of the projectile), $d\sigma_{tn}(\mathbf{q})/d^2q$ and σ_{tn} are the differential and the integral elastic cross sections for neutron scattering on the target, and $\rho(\mathbf{k}_c)$ and $\rho(\mathbf{k}_n)$ are the core and halo neutron internal momentum distributions.

It is seen that the observed core momentum distribution is equal to the internal one, while the observed transverse momentum distribution of the neutron is distorted by the interaction with the target, the longitudinal one remaining undistorted (note that the momentum transfer $\mathbf{q}$ for not-too-big values is practically perpendicular to the direction of the incoming beam). Now, if we consider diagram *2*, we shall come to similar conclusions with the roles of the neutron and the core interchanged. We see that momentum distributions of the ''participants'' of interaction with the target are distorted, while the distributions of the ''spectators'' are not. Diagram *3* corresponds to the breakup process when the target interacts with the neutron halo as well as with the core. In this case both momentum distributions of the neutron and of the core are distorted.

Expressions (3) are obtained under assumption that $\varphi_f(\mathbf{r})$ is a plane wave. However, it actually is distorted by the final-state interaction. Amplitude $F_{fi}(\mathbf{q})$ for the ''elastic'' fragmentation, corresponding to the 1st diagram, may be written in the form

$$F_{fi}(\mathbf{q}) = f_{tn}(\mathbf{q})S_{fi}(\mathbf{q}), \quad S_{fi}(\mathbf{q}) = \langle \varphi_f | \exp(i\mathbf{q}\mathbf{s}_n) | \varphi_i \rangle, \tag{4}$$

where $f_{tn}(\mathbf{q})$ is the amplitude for elastic scattering of the neutron on the target. The wave function φ_f should be orthogonal to the ground-state wave function φ_i. As a consequence of this, the inelastic formfactor $S_{fi}(\mathbf{q})$ is zero at $\mathbf{q}=0$, which is significantly different from the case when φ_f is a plane wave. Now, with a realistic φ_f, there is no direct connection between the measured momentum distributions and the internal ones.

For targets with high charge number Z, the nuclear breakup may proceed as Coulomb dissociation. The amplitude for this process at intermediate energy may be written in the form (4) with $F_{tc\,\mathrm{Coul}}(\mathbf{q})$ instead of $F_{tn}(\mathbf{q})$, where $F_{tc\,\mathrm{Coul}}(\mathbf{q})$ is the amplitude for the Coulomb scattering of the target on the core of the exotic nucleus. So, it is evident that the momentum distributions of fragments appearing due to the Coulomb dissociation are subject to final-state interaction distortions as well. In addition, they are distorted also by the strong interaction of the target with the exotic nucleus.

Another important channel of exotic-nucleus fragmentation, which is in fact dominant at sufficiently high energy, is the ''inelastic'' breakup, when the target is broken too, and new particles (primarily pions) are produced (diagram *4*). This process is often referred to as a ''stripping'' reaction.[6] The neutron knocked out from the exotic nucleus usually receives a big momentum transfer in this reaction, and it is ''absorbed'' from the elastic channel. Therefore, effects of final-state interaction are small here, and the measured momentum of the core fragment, which is a ''spectator,'' is supposed to reflect the

internal momentum of interest. However, due to the interaction of the target with the nuclear core the stripping reaction is mainly peripheral, so that the sensitivity to the momentum distribution in the nuclear interior is low, the measured momentum distributions of the core fragments of exotic nuclei being narrower than the true internal ones.[7,8]

To summarize the previous discussion, we can draw the following conclusions. The observed momentum distributions of the fragments may be distorted substantially by the interaction with the target, by the final-state interaction, and by rescattering effects. It is not possible to take the final-state interaction into account exactly since we do not know it well enough. It is not easy to take the effects of rescattering into account accurately due to the complexity of the nucleus–nucleus interaction. Information on the neutron momentum distribution in the central part of the exotic nucleus is lost because of strong absorption.

As to investigation of two-neutron halo nuclei, the situation is more complicated here. The breakup of such a nucleus may go as a suquential process. For example, in the case of fragmentation of ^{11}Li nuclei, one of the halo neutrons may be knocked out, the rest of the system being left as an intermediate excited state of the nucleus ^{10}Li, which decays to ^{9}Li and another neutron Ref. 9 (see diagram *5*). The latter is observed in the experiment in the forward direction, but the narrow transverse momentum distribution of this neutron has little to do with the internal neutron momentum distribution in ^{11}Li nuclei.

In what experiment can one obtain information on the halo neutron momentum distribution that is not distorted significantly by the reaction mechanism? Let us enumerate the requirements which, in our opinion, are demanded for such an experiment.

1. The experiment should be performed at intermediate energy. This allows one to select a direct process, to reduce distortion effects, and to have a reliable scattering theory.

2. Since the momentum distributions of ''participants'' are disturbed by interaction with the target, the ''participants'' have to be separated out, and information on the internal momentum distributions should be extracted from the ''spectators'' only. Note that in this case the transverse and longitudinal observed momentum distributions are expected to be identical.

3. To minimize the effects of the final-state interaction, the ''participants'' have to receive a sufficiently high momentum transfer.

4. For the same reason the ''participants'' should be light enough.

5. To minimize effects of distortions of momentum distributions, the target should have a small cross section for interaction with the nuclear components.

6. To minimize the contribution from Coulomb dissociation, the target should have low Z value.

7. To avoid problems of description of the nucleus–nucleus interaction, it is desirable to have the target be an elementary particle.

Below we describe an experiment that satisfies all these requirements. We propose to perform fragmentation of an exotic nucleus on a liquid hydrogen target. The appro-

priate energy of the beam may be around 300 MeV/u or somewhat higher. To be more concrete, let us consider the case of ^{11}Li. Interaction with a target proton may cause one of the halo neutrons to be knocked out from the nucleus (diagram *6*). To suppress the influence of the final-state interaction of the knocked-out neutron with the rest of the nucleus, we demand that the momentum transfer to this neutron, which is a ''participant,'' should be sufficiently high. This requirement may be satisfied by measuring the energy of the scattered target proton and selecting events for which this energy is above some value, say above 50 MeV. Note that the energy resolution of the proton detector may be rather low, since the value of the proton energy will be used only for event selection. The information on the neutron internal momentum distribution in ^{11}Li may be obtained by measuring the transverse momenta of another halo neutron and of the core-fragment ^{9}Li. From the relative transverse velocities of the detected neutron and ^{9}Li nucleus, one can obtain information on the energy of the possible intermediate resonant state of ^{10}Li. The sum of the measured transverse momenta of the neutron and of the ^{9}Li nucleus is expected to be equal to the internal momentum of the knocked-out neutron.

The proposed experiment differs from the previous experiments on fragmentation of exotic nuclei mainly in three respects. First, the fragmentation target is an elementary particle. Second, the ''participants'' in the reaction and the ''spectators'' are separated out, and only spectators whose motion is little affected by the interaction with the target are used to deduce information on the internal momentum distributions. And third, the halo neutron, which is a ''participant,'' is removed from the nucleus very quickly, so that effects of final-state interaction between this neutron and the rest of the system are small. Note also that in distinction with previous works, here it is proposed to obtain information on the halo neutron motion for two-neutron-halo nuclei not from the observed core-fragment momentum or from the forward neutron momentum alone, but from the sum of these momenta. The conditions for applicability of the ''sudden'' approximation are fulfilled (it is more correct to speak here about the ''impulse'' approximation), and the influence of rescattering effects is minimized. We believe that from this experiment one can obtain rather accurate information on the halo neutron momentum distribution. Of course, similar approach may be used for studying a halo proton momentum distribution in proton-rich nuclei, as well.

The experiment discussed may be considered as a version of the classical experiment for (p,pn) or $(p,2p)$ quasi-elastic scattering in inverse kinematics. The shell from which a nucleon is knocked off is determined in traditional (p,pn) and $(p,2p)$ experiments from the energy balance of the incident, scattered, and knocked-off nucleons. As for the present experiment, the fact that a nucleon is knocked out from the halo (but not from the core) is determined from observation of the core fragment. Strictly speaking, if we observe a core fragment, say ^{9}Li, when we consider ^{11}Li fragmentation, this does not mean that the breakup of ^{11}Li nucleus must necessarily proceed by the knock-off of a halo neutron. In principle, the breakup of the ^{11}Li nucleus may occur due to ''elastic'' scattering of the core on a target proton. However, the probability of such a process with a high momentum transfer to the core is very low. Note that the observed momentum of the ^{9}Li fragment in this case will be outside the range of interest.

An estimate of the counting rate of the events of interest for a liquid hydrogen target 10 cm long shows that rather good statistics (more than 10^5 events) may be accumulated

during a reasonable experiment time with an intensity of the beam of exotic nuclei even lower than 10^3 1/s.

The proposed experiment is discussed in more detail in Ref. 10.

[a)]e-mail: alk@hep486.pnpi.spb.ru

[1]I. Tanihata, H. Hamagaki, O. Hashimoto *et al.*, Phys. Rev. Lett. **55**, 2676 (1985).
[2]T. Nilsson, Th. Blaich, M. J. G. Borge *et al.*, Europhys. Lett. **30**, 19 (1995).
[3]T. Nilsson, F. Humbert, W. Schwab *et al.*, Nucl. Phys. A **598**, 418 (1996).
[4]A. I. Akhiezer and A. G. Sitenko, Phys. Rev. **106**, 1236 (1957).
[5]A. G. Sitenko, A. D. Polozov, M. V. Evlanov *et al.*, Nucl. Phys. A **442**, 122 (1985).
[6]R. Serber, Phys. Rev. **72**, 1008 (1947).
[7]H. Esbensen, Phys. Rev. C **53**, 2007 (1996).
[8]P. G. Hansen, Phys. Rev. Lett. **77**, 1016 (1996).
[9]F. Baranko, E. Vigezzi, and R. A. Broglia, Phys. Lett. B **319**, 387 (1993).
[10]G. D. Alkhazov, Preprint PNPI-**2167** NP-24-1997, Gatchina 1997.

Published in English in the original Russian journal. Edited by Steve Torstveit.

Measurement of the ^{45}Ca β spectrum in search of deviations from the theoretical shape

A. V. Derbin,[a] A. I. Egorov, S. V. Bakhlanov, and V. N. Muratova
St. Petersburg Institute of Nuclear Physics, Russian Academy of Sciences, 188350 Gatchina, Russia

(Submitted 9 June 1997)
Fiz. Tverd. Tela (St. Petersburg) **66**, No. 2, 81–84 (25 July 1997)

The ^{45}Ca β spectrum has been measured with a Si(Li) detector. New limits on the mixing parameter ($|U_{eH}|^2 \leqslant 0.005$) for a neutrino with mass in the interval 75–100 keV are obtained. The possibility of a monochromatic peak appearing at the end of the β spectrum is analyzed. © *1997 American Institute of Physics.*
[S0021-3640(97)00314-9]

PACS numbers: 27.40.+z, 23.40.−s

In Ref. 1, a narrow peak of relative intensity of the order of 10^{-10} and width not exceeding the spectrometer resolution was observed near the end point of the β spectrum of tritium. The negative value obtained in Ref. 2 for m_ν^2 can also be explained by the presence of a monochromatic peak of intensity of the order of 10^{-9} to the left of the limiting energy.[3] The possible unconventional reasons for the appearance of such peaks — a neutrino bound state or the existence of a neutrino sea — motivate the experimental search for similar effects in other elements which undergo β decay. At the same time, the possibility of the emission of a massive neutrino can be assessed by analyzing the shape of the β spectrum.

To observe such effects, in the present work we analyzed the spectrum of ^{45}Ca ($T_{1/2}=164$ days and $E_0 \simeq 256$ keV), which decays into the ^{45}Sc ground state (the probability of a transition to an excited level equals 0.0017%).[4] This choice of isotope was dictated by our desire to check the model proposed in Ref. 5 for the appearance of a peak at the end of the β spectrum, since the limiting energy of ^{45}Ca is very close to $m_e/2$. At the same time, the model makes it possible to study the possibility of the emission of a neutrino with mass in the interval 80–110 keV, for which the previously established limit does not exceed 10^{-2}.

The electrons were detected with a Si(Li) detector having a sensitive region 12 mm in diameter and 3 mm high. A collimator-screened ^{45}Ca source was located 25 mm from the detector surface. The peak near the end of the β spectrum can be simulated by natural or artificial radioactivity and the massive-neutrino emission effect can be simulated by the Compton-scattering edge. For this reason, precise measurements require β sources of extremely high radioactive purity. Such sources were specially prepared for the present experiment. For three weeks 2 mg $CaCO_3$, enriched to 13% with the isotope ^{44}Ca and containing less than 1% ^{40}Ca, were irradiated in a reactor with a flux of 10^{13} neutrons/$cm^2 \cdot s$. After eight weeks, when the ^{47}Ca activity had mostly decayed, the calcium car-

bonate was dissolved in a drop of dilute nitric acid. The calcium ions were collected at the top of an ion-exchange column with a cationite in NH_4 form. The column was washed with a 0.01 M solution of ammonium nitriloacetate with a pH of 7.8 and water, after which the ^{45}Ca was washed out with a nitric acid solution with acidity increasing continuously from 0.1 to 2 M. The emergence of the ^{45}Ca peak was checked according to the residual γ activity of ^{47}Ca. The chromatographic purification operation was repeated twice, after which the calcium solution was evaporated to a drop and allowed to stand for 120 days to let the residual ^{47}Ca activity decay ($T_{1/2}=4.5$ days).

In our experimental detector–source geometry the deviation of the resolution function from a Gaussian is mainly determined by the back diffusion of electrons from the detector surface as well as by electron energy losses in the source or the insensitive layer of the detector. To determine this function, the free isotope ^{125m}Te, purified by the procedure described in Ref. 6, was added to ^{45}Ca and isotropically mixed. The energies of the two main conversion lines of ^{125m}Te are equal to 77.5 and 104.4 keV.

To prepare a working β source, a lithium aluminate sorbing spot 10 mm in diameter was produced on 4-μm thick aluminum foil. When the calcium nitrate solution was deposited on the sorbing layer, ^{45}Ca and ^{125m}Te were uniformly trapped by the surface and $LiNO_3$ was pulled to the edges of the spot which were screened by the collimator. After preparation, the source was placed in a vacuum cryostat containing the Si(Li) detector. For this, the background spectrum of the detector was measured and found to be described well by a linear function in the interval 100–270 keV. The detector had a preamplifier with a continuous drain feedback and with a cooled field-effect transistor, an amplifier with a formation time constant of 2 μs, a circuit for screening pulse overlaps with a temporal resolution of 0.3 ns, and a 12-digit ADC graduated to 80 eV/channel. The input load was equal to 150 Hz. With an overlap screening time of 0.3 ns the result was that the entire background was due to the natural or artificial radioactivity. The resolution of the detector measured according to the 77 keV conversion-electron line was equal to 1.6 keV, and the shift of this line on the energy scale, calibrated with respect to the ^{57}Co and ^{241}Am γ lines, was equal to 0.4 keV. Therefore the difference in the energy losses of the 120 and 270 keV electrons did not exceed 200 eV.

A total of 8×10^8 ^{45}Ca decays were detected. The experimental spectrum was compared with the theoretical spectrum by searching for a minimum of the χ^2 functional. First, two parameters of a linear approximation of the background were found for the interval 259–270 keV; these parameters were used for the entire spectrum and not varied. Actually, the background from the natural radioactivity was described by these two parameters, since the background due to pulse overlap was an order of magnitude weaker. The rest of the spectrum was compared with the formula

$$N(E_i)=A\sum_k F(E_k,Z)S(E_k,E_0,U_{eH},M_\nu)R(E_i,E_k), \tag{1}$$

where A is a normalization constant, $F(E_k,Z)$ is the Coulomb function taking account of the screening correction, $S=(1-|U_{eH}|^2)S(M_\nu=0)+|U_{eH}|^2S(M_\nu=M_H)$ is the sum of two β-spectra with limiting energy E_0 and neutrino mass M_ν, and $R(E_i,E_k)$ is the experimentally determined resolution function for the 77 keV conversion line. A term proportional to $\alpha\Sigma N(E_i)/E_i$ and representing a sum of the constant tail of the resolution

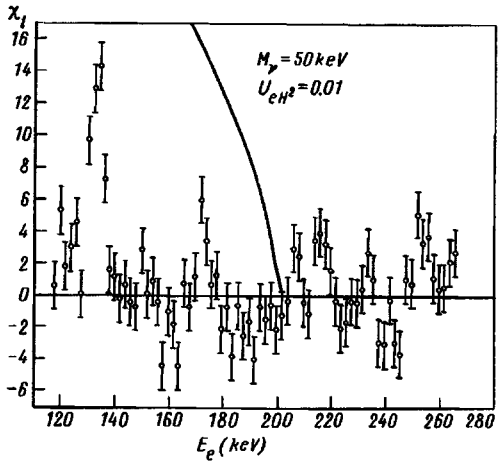

FIG. 1. Optimal fit in the interval 140–270 keV for $|U_{eH}|^2=0$. The value of a channel is 1 keV. The solid curve shows the additional contribution obtained with fixed parameters of the fitting procedure for $M_\nu=50$ keV, and $|U_{eH}|^2=0.01$.

function, whose intensity α could not be found from the measured spectrum and therefore was varied as a free parameter, was added to the function $N(E_i)$. Four parameters were varied — the end-point energy E_0, A, M_ν, and α. This fitting procedure gives an acceptable value of χ^2 in the interval 140–270 keV. The χ_i curve for the optimal fit ($M_H=0$) is shown in Fig. 1. The position of the lower limit of the interval determined the appearance of a wide peak with energy 132 keV. This peak is due to coincidences between the conversion and Auger electrons and x- and γ-rays emitted in two successive transitions in ^{125m}Te (Ref. 6).

The value of E_0 was determined to be 256.6(2) keV. The solid curve shows the additional contribution to the spectrum for the case when a neutrino with a mass of 50 keV is emitted with probability 5×10^{-2} per decay. The emission probability for different neutrino masses M_ν was determined by constructing a χ^2profile. Figure 2 displays a curve of the limit on the probability of mixing of a heavy neutrino in the interval 20–160 keV (90% confidence level) in comparison with other experiments.[7–9] Therefore the new limit on the mixing parameter in the neutrino mass interval 75–100 keV is $|U_{eH}|^2\leqslant0.005$.

The observation of a monochromatic peak in the continuous spectrum is a more model-independent problem than is the search for a contribution from a smoothly increasing function in the case of the emission of a heavy neutrino. The maximum likelihood method was also used to search for a monochromatic peak near the limiting energy. The experimentally determined function for 77 keV conversion electrons with a tail found for the optimal fit in the interval 140–270 keV was used as the response function of the detector. The results of the fitting procedure in the interval 250–260 keV are displayed in Fig. 3. It was found that the probability for the appearance of a monochromatic peak near the limiting energy ($E_0\pm3$ keV) is less than $(2.0–0.7)\times10^{-7}$ events per decay. Figure 3 shows a section of the spectrum in the indicated interval and displays the results of the

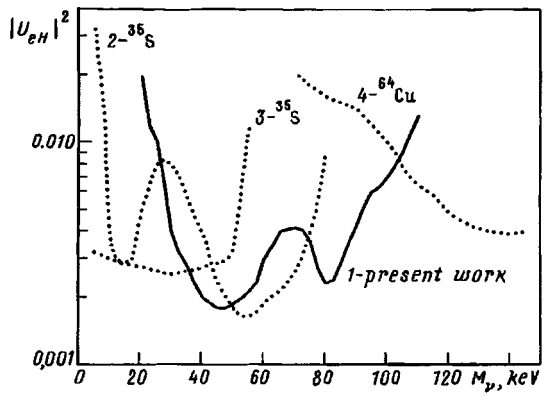

FIG. 2. Limit on the mixing parameter $|U_{eH}|^2$ (90% confidence level) obtained in the present experiment (curve *1*). The curves *2*, *3*, and *4* correspond to the limits from Refs. 7–9.

fitting procedure in the case when there is no peak and for a monochromatic peak with an intensity of 5×10^{-7}. The limit on the intensity of the peak with energy equal to the limiting energy of the ^{45}Ca β-decay was equal to 1.3×10^{-7} per decay (90% confidence level). The achieved sensitivity to a monochromatic peak at the end of the β spectrum is appreciably worse than the result obtained in Ref. 1, but at the same time the limit obtained attests to the absence (at the 10^{-7} level) of resonance end-point peak enhancement due to the fact that $E_0=m_e/2$.

We are grateful to O. I. Sumbaev for initiating this work and for suggesting that a mixed β-source containing conversion-electron calibration lines be prepared.

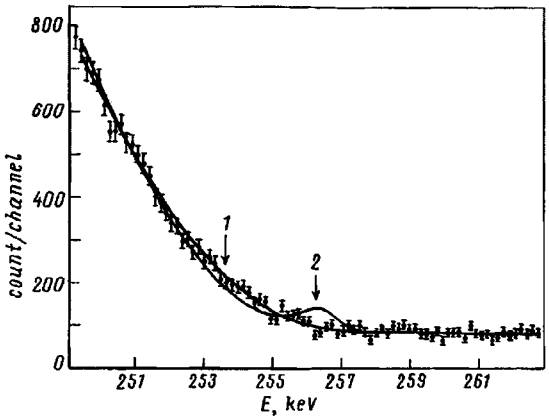

FIG. 3. Results of the fitting procedure in the interval 250–260 keV (80 eV/channel). Curve *1* — absence of a peak ($\chi^2_n=1.07$), curve *2* — peak with intensity 5×10^{-7} per decay ($\chi^2_n=1.96$).

[a)]e-mail: derbin@lnpi.spb.su

[1] A. I. Belesev *et al.*, Phys. Lett. B **350**, 263 (1995).
[2] R. M. Barnett *et al.*, Phys. Rev. D **54**, 238 (1996).
[3] W. Stoeffl and D. J. Decman, Phys. Rev. Lett. **75**, 3237 (1995).
[4] C. M. Lederer and V. S. Shirley, *Table of Isotopes*, Wiley, New York, 1978.
[5] O. I. Sumbaev, Dokl. Akad. Nauk SSSR **316**, 1116 (1991) [Sov. Phys. Dokl. **36**, 165 (1991)]; Preprint NN 1551, 1637, 1811, Leningrad Institute of Nuclear Physics.
[6] A. V. Derbin, A. I. Egorov, I. A. Mitropol'skiĭ *et al.*, JETP Lett. **65**, 605 (1997).
[7] A. M. Apalikov, S. D. Boris, A. I. Golutvin *et al.*, JETP Lett. **42**, 289 (1985).
[8] J. Markey and F. Boehm, Phys. Rev. **32**, 2215 (1985).
[9] K. Schreckenbach, G. Colvin, and F. von Feilitzsch, Phys. Lett. B **129**, 265 (1983).

Translated by M. E. Alferieff

Liouville theory on a Z_N Riemann surface

S. A. Apikyan[a)]
Erevan Physics Institute, 375036 Erevan, Armenia

(Submitted 22 May 1997; resubmitted 20 June 1997)
Pis'ma Zh. Éksp. Teor. Fiz. **66**, No. 2, 85–90 (25 July 1997)

Liouville field theory on a Z_N curve is studied. It is shown that the partition function on such surfaces reduces to Liouville correlation functions on a sphere and to a free scalar theory with Ramond boundary conditions. © *1997 American Institute of Physics.* [S0021-3640(97)00414-3]

PACS numbers: 11.10.Kk, 02.40.Ky

Despite the great interest in Liouville theory (due to its relation to string theory), many problems in this field of inquiry remain open. In recent years, the appearance of Refs. 1–3, where analytical expressions were constructed for the Liouville structure constants, has rekindled interest in it.

This letter is concerned with the manifestation of the conformal properties of Liouville theory on a Riemann surface possessing Z_N symmetry. It is shown that the partition function of the Liouville theory on a Z_N Riemann surface reduces to the correlation functions of a Liouville theory on a sphere and to the correlation functions of the twist fields.

The Z_N-symmetric Riemann surfaces $X_g^{(N)}$ of genus $g \geqslant 1$ are determined by algebraic equations of the form

$$y^N(z)=\prod_{i=1}^{h}(z-\omega_i)^{n_i}, \quad n_i>1, \tag{1}$$

i.e., $X_g^{(N)}$ is an N-sheet covering of a Riemann sphere. The genus g of a Z_N Riemann surface

$$g=(N-1)(h-2)/2 \tag{2}$$

can be calculated via the Riemann–Hurwitz theorem. A Riemann surface with Z_N symmetry possesses h complex parameters, and therefore the dimension of the moduli space $\mathcal{M}_{Z_N}$ is

$$\dim \mathcal{M}_{Z_N}=h-3=\frac{2g}{N-1}-1. \tag{3}$$

Comparing with the dimension of the moduli space $\mathcal{M}$ of a Riemann surface of the general position

$$\dim \mathcal{M}=\begin{cases}1, & g=1\\ 3g-3, & g>1\end{cases}, \tag{4}$$

we can conclude that a Z_N Riemann surface does not fill all Riemann surfaces.

Let us consider the Liouville theory in the conformal gauge. The Liouville Lagrangian density on surfaces can be represented as

$$\mathcal{L}=\frac{1}{4\pi}(\partial_a\phi)^2+\mu e^{2b\phi}+\frac{Q}{4\pi}\hat{R}\phi, \tag{5}$$

where b and μ are, respectively, the coupling constant and the cosmological constant. We fixed the metric $\hat{g}$ on a given topological surface with curvature $\hat{R}$, normalized as

$$\frac{1}{4\pi}\int\sqrt{\hat{g}}\hat{R}=2(1-g) \tag{6}$$

on a genus-g surface.

We enumerate the N sheets of a Z_N Riemann surface $X_g^{(N)}$ with the numbers $l=0, 1, \ldots, N-1$ and we represent each sheet as

$$y^{(l)}(z)=\omega^l\prod_{j=1}^{h}(z-\omega_j)^{n_j/N}, \tag{7}$$

where $\omega=e^{2\pi i/N}$ is the Nth root of unity.

Under the transformation (7) the Lagrangian density, the energy–momentum tensor, and the Liouville field ($\mathcal{L}(\phi(y))$, $T(\phi)$, and $\phi(y)$, respectively) on a Z_N Riemann surface $X_g^{(N)}$ transfer to the branches $\mathcal{L}^{(l)}(\phi^{(l)}(z))$, $T^{(l)}(z)$, and $\phi^{(l)}(z)$ ($l=0, 1, \ldots, N-1$). Each branch of the Liouville fields $\phi^{(l)}(z)$ transforms under holomorphic transformations as the logarithm of a conformal factor of the metric

$$\phi^{(l)}(\omega,\overline{\omega})=\phi^{(l)}(z,\overline{z})-\frac{Q}{2}\log|\omega'(z)|^2, \tag{8}$$

where

$$Q=b+1/b. \tag{9}$$

On each sheet we have a holomorphic Liouville energy–momentum tensor

$$T^{(l)}(z)=-(\partial\phi^{(l)}(z,\overline{z}))^2+Q\partial^2\phi^{(l)}(z,\overline{z}) \tag{10}$$

with the Liouville central charge

$$\hat{c}=1+6Q^2. \tag{11}$$

Let the fields ($T^{(l)}(z)$, $\phi^{(l)}(z,\overline{z})$) on a N-sheet covering be vector fields on CP^1. When the arguments of the field make a circuit around a branch point, the vector fields are transformed by a monodromy matrix. Monodromy matrices form a representation of the homotopic group $\pi_1(CP^1/\cup\omega_j)$, and in our case they are simply identical to the group Z_N.

For convenience, we now switch to the basis employed in Ref. 4. The generators of the monodromy group become diagonal in this basis:

$$\phi_{(k)}(z,\overline{z})=\sum_{l=0}^{N-1}\omega^{-kl}\phi^{(l)}(z,\overline{z}),$$
$$T_{(k)}(z)=\sum_{l=0}^{N-1}\omega^{-kl}T^{(l)}(z). \tag{12}$$

The ''bosonization rules'' for $T_{(k)}$ in a diagonal basis can be represented as

$$T_{(k)}=-\frac{1}{N}\sum_{s=0}^{N-1}\partial\phi_{(s)}\partial\phi_{(k-s)}+Q\partial^2\phi_{(k)}. \tag{13}$$

In particular, the Liouville energy–momentum tensor can be represented as

$$T_{(0)}=-\frac{1}{N}\partial\phi_{(0)}\partial\phi_{(0)}+Q\partial^2\phi_{(0)}-\frac{1}{N}\sum_{s\neq 0}\partial\phi_{(s)}\partial\phi_{(-s)}, \tag{14}$$

and the corresponding central charge is

$$c=N(1+6Q^2). \tag{15}$$

Expression (14) and (15) make obvious the splitting of the initial theory into a Liouville theory on a sphere with central charge $c_s=1+6Q^2N$ and a free scalar theory of the fields $\phi_{(s)}$ $(s=1,2,\ldots,N-1)$ with the $(N-1)$st central charge $c_f=1$. Under a holomorphic transformation of the coordinates the Liouville field $\phi_{(0)}\equiv\Phi$ and the free fields $\phi_{(k)}$ $(k\neq 0)$ transform as

$$\Phi(\omega,\overline{\omega})=\Phi(z,\overline{z})-\frac{N}{2}Q\,\log|\omega'(z)|^2,$$
$$\phi_{(k)}(\omega,\overline{\omega})=\phi_{(k)}(z,\overline{z}),\quad k\neq 0. \tag{16}$$

We now rewrite expression (14) in the new notation as

$$T=-\frac{1}{N}\partial\Phi\partial\Phi+Q\partial^2\Phi-\frac{1}{N}\sum_{s\neq 0}^{N-1}\partial\phi_{(s)}\partial\phi_{(-s)}. \tag{17}$$

In accordance with the properties of monodromy[4] of vector fields on CP^1, we must determine Liouville vertex operators of two types. The first type are the so-called non-twisted vertex operators

$$V_{[0]}(z,\overline{z})=\exp\{2\alpha\Phi(z,\overline{z})\}\exp\left\{i\sum_{s\neq 0}\alpha_{(s)}\phi_{(s)}(z,\overline{z})\right\} \tag{18}$$

with dimension

$$\Delta_{\alpha,\beta}=2\alpha(Q-\alpha)+\frac{N}{2}\sum_{s\neq 0}\alpha_{(s)}\alpha_{(-s)}. \tag{19}$$

The physical state space of the Liouville theory is well known and is determined by the charge[5,6]

$$\alpha=ip+Q/2. \tag{20}$$

Therefore we obtain as the final expression for the dimension of the nontwisted vertex operators

$$\Delta=\frac{Q^2}{2}+2p^2+\frac{N}{2}\sum_{s\neq 0}\alpha_{(s)}\alpha_{(-s)}. \tag{21}$$

The second type are the twisted Liouville vertex fields of the form

$$V_{[k]}(z,\overline{z})=\exp\{2\gamma\Phi(z,\overline{z})\}\sigma_k(z|1)\sigma_k(z|2)\ldots\sigma_k(z|N-1) \tag{22}$$

with the corresponding dimension[4]

$$\Delta_{[k]}=2\gamma(Q-\gamma)+(N^2-1)/24\,N. \tag{23}$$

The dimensions of the twist fields $\sigma_k(z|l)$ are

$$\Delta_{kl}=\frac{1}{4}\left[\left\{\frac{kl}{N}\right\}-\left\{\frac{kl}{N}\right\}^2\right], \tag{24}$$

where the symbol $\{x\}$ denotes the fractional part of x.

Our aim now is to construct, on the basis of this knowledge, the partition function of the Liouville theory on the surface $X_g^{(N)}$. According to Polyakov's conjecture,[7] summation over a smooth metric with inserted vertex operators is equivalent to summation over a metric with singularities at the points of the inserted vertex operators. Therefore the partition function of the Liouville theory on a Riemann surface

$$Z_g=\int D\phi\,\exp\left[-\int\frac{1}{4\pi}(\partial_a\phi)^2+\mu e^{2b\phi}+\frac{Q}{4\pi}\hat{R}^g\phi\right] \tag{25}$$

can be represented on a Z_N Riemann surface as

$$\begin{aligned}Z_g=&\int D\Phi\,\exp\left[-\int\frac{1}{4\pi N}(\partial_a\Phi)^2+\mu e^{2b\Phi}+\frac{Q}{4\pi}\hat{R}^{g=0}\Phi\right]\\&\times\prod_{s\neq 0}D\phi_{(s)}\,\exp\left[-\int\frac{1}{4\pi N}\sum_{s\neq 0}\partial\phi_{(s)}\partial\phi_{(-s)}\right]\\&\times\prod_{i=1}^{h}\exp\{2\gamma_i\Phi(\omega_i,\overline{\omega_i})\}\sigma_{k_i}(\omega_i|1)\sigma_{k_i}(\omega_i|2)\ldots\sigma_{k_i}(\omega_i|N-1),\end{aligned} \tag{26}$$

where

$$b=\frac{Q}{2}\pm\sqrt{\frac{Q^2}{4}-\frac{1}{2}}. \tag{27}$$

To calculate the last partition function, first we integrate over the zero modes of the Liouville fields Φ. After integrating over the zero modes we obtain (in variable fields orthogonal to the zero modes[8])

$$Z_g=(-\mu)^s\frac{\Gamma(-s)}{b}\int D\widetilde{\Phi}\,\exp\left[-\int\frac{1}{4\pi N}(\partial\widetilde{\Phi})^2+\frac{Q}{4\pi}\hat{R}^{g=0}\widetilde{\Phi}\right]$$

$$\times\left(\int e^{2b\tilde{\Phi}}\right)^s \prod_{i=1}^{h} \exp\{2\gamma_i\tilde{\Phi}(\omega_i,\overline{\omega_i})\}\int\prod_{s\neq 0} D\phi_{(s)}$$

$$\times\exp\left[-\int\frac{1}{4\pi N}\sum_{s\neq 0}\partial\phi_{(s)}\partial\phi_{(-s)}\right]\prod_{i=1}^{h}\sigma_{k_i}(\omega_i|1)\sigma_{k_i}(\omega_i|2)\ldots\sigma_{k_i}(\omega_i|N-1), \tag{28}$$

where

$$\sum_{i=1}^{h}\gamma_i = Q - sb. \tag{29}$$

The last integral expression (the correlation function) of the fields σ_k in Eq. (28) is defined as

$$\left\langle\prod_{i=1}^{h}\sigma_{k_i}(\omega_i|1)\sigma_{k_i}(\omega_i|2)\ldots\sigma_{k_i}(\omega_i|N-1)\right\rangle = \prod|\omega_i-\omega_j|^{-2\gamma_{ij}}(\det\hat{W})^{-1/2}, \tag{30}$$

where $\hat{W}$ is the matrix of periods, and γ_{ij} forms a basis in $H_1(X_g^{(N)},Z)$ (Ref. 9). Moreover, it is well known that the multipoint correlation function (30) reduces to the partition function of a free scalar theory with Ramond boundary conditions.[10]

The first integral (correlation function) in Eq. (28) is not a free-field correlation function, since in the general case the degree s is not positive and integral. But if s assumes integral values $s=n=0, 1, 2, \ldots$, then the partition function Z_g possesses poles at $\Sigma\gamma_i$ with residues equal to the corresponding perturbative integrals

$$\sum_{\gamma_{i=Q-nb}}\ \operatorname{Res} Z_g(\omega_1,\ldots,\omega_h) = G^{(n)}(\omega_1,\ldots,\omega_h)\Big|_{\sum\gamma_i=Q-nb}, \tag{31}$$

where $G^{(n)}$ is a free-field correlation function

$$G^{(n)} = \frac{(-\mu)^n}{n!}\int D\Phi\,\exp\left\{-\int\frac{1}{4\pi N}(\partial\Phi)^2 + Q\hat{R}^{g=0}\Phi\right\}\prod_{j=1}^{n}\int\sqrt{\hat{g}}$$

$$\times\exp\{2b\Phi(x_j)\}d^2x_j\prod_{i=1}^{h}\exp\{2\gamma_i\Phi(\omega_i,\overline{\omega_i})\}\int\prod_{s\neq 0}D\phi_{(s)}$$

$$\times\exp\left[-\frac{1}{4\pi N}\int\sum_{s\neq 0}\partial\phi_{(s)}\partial\phi_{(-s)}\right]\prod_{i=1}^{h}\sigma_{k_i}(\omega_i|1)\sigma_{k_i}(\omega_i|2)\ldots\sigma_{k_i}$$

$$\times(\omega_i|N-1), \tag{32}$$

which is the nth term in the naive expansion (26) for Z_g in powers of μ. So, the partition function of the Liouville theory on a Z_N Riemann surface reduces to the Liouville correlation function on a sphere with inserted Liouville vertex operators (with charges γ_i) and a correlation function of the twist fields.[11] Therefore the residues of the partition function of the Liouville theory on a Z_N Riemann surface at the poles $\Sigma\gamma_i=Q-nb$ are identical to the correlation function of the free-field theory on a Z_N Riemann surface.

Let us now examine the particular case of a Liouville theory on an elliptical curve, i.e., $N=2$, $h=4$. We rewrite expression (26) in this particular case as

$$Z_1=\int D\Phi\ \exp\left[-\int \frac{1}{8\pi}\,(\partial_a\Phi)^2+\mu e^{2b\Phi}+\frac{Q}{4\pi}\,\hat{R}^{g=0}\Phi\right]D\phi$$

$$\times\exp\left[-\int \frac{1}{8\pi}\,\partial\phi\partial\phi\right]\prod_{i=1}^{4}\ e^{2\gamma_i\Phi(\omega_i,\overline{\omega_i})}\sigma_{\epsilon_i}(\omega_i,\overline{\omega_i}). \tag{33}$$

Then the residue of Z_1 will be equivalent to the four-point function

$$\sum_{\gamma_{i=Q-nb}}\ \text{Res}\quad Z_1(\omega_1,\ldots,\omega_4)=G^{(n)}(\omega_1,\ldots,\omega_4)\Big|_{\sum\ \gamma_i=Q-nb} \tag{34}$$

where $G^{(n)}$ has the form

$$G^{(n)}_{\gamma_1,\gamma_2,\gamma_3,\gamma_4}(\omega_1,\omega_2,\omega_3,\omega_4)$$

$$=\frac{(-\mu)^n}{n!}\int D\Phi e^{-\int\frac{1}{8\pi}(\partial\Phi)^2+Q\hat{R}^{g=0}\Phi}\prod_{j=1}^{n}\int\sqrt{\hat{g}}e^{2b\Phi(x_j)}d^2x_j\prod_{i=1}^{h}\ e^{2\gamma_i\Phi(\omega_i,\overline{\omega_i})}$$

$$\times\int_{\phi\in S^1}D\phi\ \exp\left[-\frac{1}{8\pi}\int\partial\phi\partial\phi\right]\prod_{i=1}^{4}\ \sigma_{\epsilon_i}(\omega_i,\overline{\omega_i}). \tag{35}$$

Therefore the Liouville partition function on an elliptical curve reduces to a four-point correlation function on a sphere of Liouville vertex operators and to the partition function of a free scalar theory, where the integration extends over compactified fields with Ramond boundary conditions.

[a)]e-mail: apikyan@1x2yerphi.am

[1] H. Dorn and H. Otto, Phys. Lett. B **291**, 39 (1992).
[2] H. Dorn and H. Otto, Nucl. Phys. B **429**, 375 (1994).
[3] A. B. Zamolodchikov and Al. B. Zamolodchikov, hep-th/9506136.
[4] S. A. Apikyan and C. Efthimiou, hep-th/9610051.
[5] T. Curtright and C. Thorn, Phys. Rev. Lett. **48**, 1309 (1982); E. Braaten, T. Curtright, and C. Thorn, Phys. Lett. B **118**, 115 (1982); Ann. Phys. **147**, 365 (1983).
[6] J. Gervais and A. Neveu, Nucl. Phys. B **238**, 125 (1984); B **238**, 396 (1984), B **257**, [FS14], 59 (1985).
[7] L. Takhtajan, ''Semiclassical Liouville theory. Complex geometry of moduli space and uniformization of the Riemann surface'' in *New Symmetry Principles in Quantum Field Theory*, edited by J. Frolich *et al.*, Plenum Press, New York, 1992.
[8] M. Goulian and M. Li, Phys. Rev. Lett. **66**, 2051 (1991).
[9] M. Bershadsky and A. Radul, Int. J. Mod. Phys. A **2**, 165 (1987).
[10] V. Knizhnik, Commun. Math. Phys. **112**, 567 (1987).
[11] Al. B. Zamolodchikov, Nucl. Phys. B **285**, [FS19], 481 (1987); L. Dixon, D. Friedan, E. Martinec, and S. Shenker, Nucl. Phys. B **282**, 13 (1987). C. Crnkovic, G. Sotkov, and M. Stanishkov, Phys. Lett. B **220** 397 (1989); S. A. Apikyan and C. J. Efthimiou, Phys. Lett. B **359**, 313 (1995). S. A. Apikyan and Al. B. Zamolodchikov, Zh. Éksp. Teor. Fiz. **92**, 34 (1987) [Sov. Phys. JETP **65**, 19 (1987)].

Translated by M. E. Alferieff

Shock wave structure in dense gases

V. V. Zhakhovskii[a)]
Institute for High Temperatures, Russian Academy of Sciences, 127412 Moscow, Russia

K. Nishihara
Institute of Laser Engineering, Osaka University, 565 Osaka, Japan

S. I. Anisimov
Landau Institute of Theoretical Physics, Russian Academy of Sciences, 117940 Moscow, Russia

(Submitted 6 June 1997; resubmitted 26 June 1997)
Pis'ma Zh. Éksp. Teor. Fiz. **66**, No. 2, 91–96 (25 July 1997)

The internal structure of a shock wave front in a gas is studied by molecular dynamics (MD) simulation. A new approach to MD shock simulation is used, which enables one to consider a stationary shock front at rest and radically improves the quality of simulation. The profiles of flow variables and their fluctuations are calculated. The evolution of the velocity distribution function across the shock layer is calculated and compared with the bimodal distribution. The pair distribution function in the shock layer is determined. The surface tension associated with the shock wave is estimated. © *1997 American Institute of Physics.* [S0021-3640(97)00514-8]

PACS numbers: 52.35.Tc, 51.10.+y, 02.70.Ns

The shock wave is a principal element of gas-dynamic flows. Since the changes of the flow parameters across a shock wave front are uniquely determined by the conservation laws and do not depend on the internal structure of the front, the shock wave is considered in gas dynamics as a structureless discontinuity. In the kinetic theory, the shock wave is treated as a transition layer of finite thickness, and its internal structure is of particular interest. For the most part, shock-wave structure studies have been performed either in the hydrodynamic approximation[1–3] (which is valid for weak shocks) or on the basis of the Boltzmann transport equation (which holds for low-density gases[4–9]). The first gas kinetic analysis of strong shock wave structure was carried out in Refs. 4 and 5 using the so-called bimodal approximation. It is assumed that the distribution function within the wave may be represented as a linear combination of two Maxwellian distributions corresponding to uniform upstream and downstream flows:

$$f(\mathbf{v},z)=(1-\alpha(z))f_1(\mathbf{v})+\alpha(z)f_2(\mathbf{v}), \tag{1}$$

where $f_i(\mathbf{v})$ is the Maxwellian distribution with the particle number density n_i, mass velocity $\mathbf{u}_i$, and temperature T_i $(i=1,2)$. The subscripts 1 and 2 denote the uniform upstream and downstream conditions, respectively. The distribution function (1) does not satisfy the Boltzmann equation. Various equations have been proposed in the literature[7] to determine $\alpha(z)$. A comparison with experimental data shows reasonable accuracy of

the bimodal approximation (1), but gives no way to decide which of the equations proposed in the literature yields better results. Note that some of the results concerning the shock front structure obtained using the Boltzmann equation are in conflict with those obtained in the framework of the hydrodynamic equations. For example, in the hydrodynamic approximation[1] the density approaches its limiting values n_1 and n_2 exponentially as $|z|\to\infty$, whereas the solution of the Boltzmann equation for weak shock wave[10,11] shows a different asymptotic behavior. It is conceivable that this discrepancy might be attributed to the fact that only two-particle collisions are taken into account in the Boltzmann equation.

To calculate the shock front structure in solids, liquids, and dense gases the molecular dynamics method and the direct Monte Carlo simulation approach have been employed.[9,12–15] These simulation studies have several shortcomings, however. In the majority of MD simulations a plane shock wave is generated by a piston compressing a fluid which is initially at rest. The resulting shock wave is unsteady. This approach, along with small number of particles in the simulation box, leads to unduly high level of nonphysical fluctuations.[12–14] As a result, there is no way to calculate the velocity distribution function within the shock front with sufficient accuracy. In Ref. 14, for example, qualitative statements as to the presence of anisotropy and non-Maxwellian character of the velocity distribution inside the shock front are based on calculation of the moments of the velocity distribution. Notice that the interpretation of the simulation results in Refs. 12–15 and other similar works is usually carried out in terms of hydrodynamic variables, some of which lose their meaning on a molecular scale.

In this work several physical problems related to the internal structure of shock waves are solved. First, we calculated local velocity distributions at several points within the shock front. Second, we found the asymptotic behavior of the hydrodynamic variables in the shock wave. Third, we calculated an additional pressure resulting from shock front curvature (the effect similar to the surface tension). We consider a shock front which is at rest in a laboratory frame. A special potential configuration is used which accelerates the gas at one side of the MD cell and decelerates it at the opposite side. As a result, a stationary shock wave is formed inside the cell, and the level of fluctuations significantly decreases, as will be shown below.

We describe the interaction of atoms by the Lennard-Jones potential: $U(r)=4\varepsilon[(\sigma/r)^{12}-(\sigma/r)^6]$. We will use the MD units defined in the standard way[16] in terms of the values of ε and σ. The rectangular MD cell $L_x\times L_y\times 2L_z$ has dimensions of $56\times 56\times 240$ units. The total number of particles is 32000. The flow velocity $v(z)<0$ is directed along the z axis. Periodic boundary conditions are imposed along the three coordinate axes. The short-range potentials U^+ and U^- are located at $z=\pm L_z$ and satisfy the condition that the forces $\partial U^+/\partial z=\partial U^-/\partial z=0$. Since the accelerating U^+ and decelerating U^- potentials have different magnitudes, the particles crossing the boundary $z=\pm L_z$ change their energy.

To form a uniform upstream flow with given temperature T_1 and mass velocity v_1, the Langevin thermostat[17] is used. The thermostat constitutes a part of the MD cell (located in the region $100<z<116$) in which the atoms are subjected to a Langevin force

$$F_k^a(t)=R_k^a(t)-\beta(v_k^a-v_1\delta_{kz}), \tag{2}$$

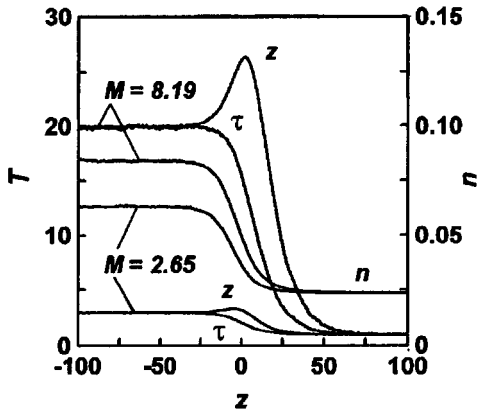

FIG. 1. Density profiles in the shock front (n) and mean-square fluctuations of the longitudinal (z) and transverse (τ) molecular velocity components.

where the subscript $k=x, y, z$, the superscript a enumerates the atoms, β is the friction coefficient, and $R_k^a(t)$ is Gaussian random force. To obtain a prescribed temperature T_1 the parameters of Eq. (2) must satisfy the condition $\langle R^2\rangle = 2\beta T_1/\Delta t$, where Δt is the time step of the integration. The equations of motion are integrated using the 8th order Stoermer method. The details of the algorithm are described in Ref. 18. The accuracy of the calculations may be characterized by the relative amplitude of the fluctuations of the total energy and center-of-mass position. In our calculations these amplitudes were less than 0.5%.

Going to the discussion of the results of simulations, we consider a typical case of a shock wave of moderate intensity (Mach number $M=12v_1/\sqrt{5}T_1\approx 5.4v_1$) in a gas of moderate density. The parameters of shock waves at Mach numbers 2.65 and 8.19 are specified as:

(a) $v_1=-0.49$, $n_1=0.0235$, $T_1=0.992$,
$v_2=-0.181$, $n_2=0.0632$, $T_2=2.97$;

(b) $v_1=-1.50$, $n_1=0.0235$, $T_1=0.983$,
$v_2=-0.42$, $n_2=0.0837$, $T_2=19.96$.

The interatomic distance and the mean free path of atoms in the upstream flow are of the same order of magnitude: $d_1\approx 3.5$ and $\lambda_1\approx 6.4$ in case (b). The parameters of uniform supersonic and subsonic flow satisfy the Hugoniot equation calculated using the equation of state data for argon taken from Ref. 19.

The number density profile within the shock front is shown in Fig. 1. The shock wave thickness defined as $\delta=(n_2-n_1)/|dn/dz|_{\max}$ is in agreement with experimental data cited in Ref. 14. As was noted above, in the hydrodynamic approximation the differences $n(z)-n_1$ and $n_2-n(z)$ decrease exponentially as $|z|\to\infty$. Analysis based on the Boltzmann equation[10,11] suggests that the above differences are proportional to

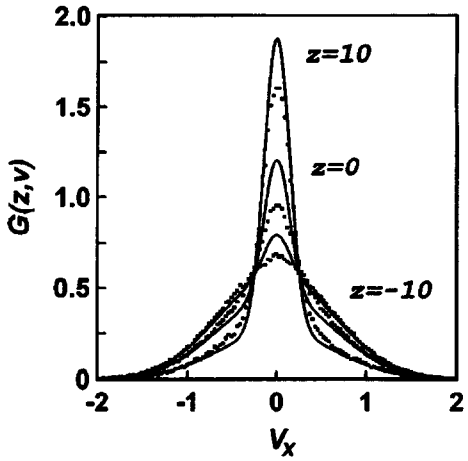

FIG. 2. Variation of the velocity distribution functions $G_d(z,v_x)$ and $G_b(z,v_x)$ in the shock front at $M=8.19$.

$\exp(-k|z|^m)$ with $m<1$. It follows from the simulation results that $m=1.01\pm0.03$. This result can be considered as evidence that the kinetic approach[10,11] is not applicable to the description of the asymptotic behavior of the flow variables at $|z|\to\infty$. It would be instructive, however, to compute the exponent m using a larger MD cell.

The temperature profiles inside the shock front shown in many papers make no physical sense because the temperature is not defined for nonequilibrium states. The quantity that is well defined is the mean-square fluctuation of the particle velocity (which is equal to the temperature at equilibrium). The simulation reveals that the fluctuations of the longitudinal (v_z) and transverse (v_x, v_y) velocity components show quite different behavior (Fig. 1). When moving in the direction from upstream toward downstream, the fluctuation $\langle(v_z-\overline{v_z})^2\rangle$ first increases rapidly, then passes through a maximum, and approaches its downstream value from above. The fluctuation $\langle v_x^2\rangle$ increases more slowly and monotonically from its upstream to downstream value. To understand this behavior we note that the transformation of the energy of ordered motion along the z axis into the energy of random motion along the x axis requires large-angle scattering, which occurs when the particle velocity is large. Therefore, this process leads primarily to the generation of high-energy tails in the distributions of particles over v_x and v_y, and the rate of energy transformation is rather low. The randomization of the z component of the velocity is not much connected with the tails of distribution function and has a higher rate.

The evolution of the particle distributions over the velocity components inside the shock front is shown in Figs. 2 and 3. The distribution functions are defined as

$$F(z,v_z)=\int f(z,\mathbf{v})dv_x dv_y, \quad G(z,v_x)=\int f(z,\mathbf{v})dv_y dv_z.$$

The simulation results (dots, subscript d) are compared with the bimodal distribution (1) (solid lines, subscript b) for different thin layers normal to the z axis. All the distribution functions are normalized to unity. As is seen from Fig. 2, the evolution of the v_x distri-

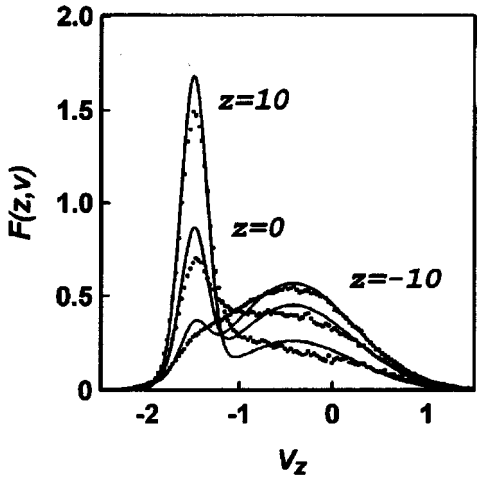

FIG. 3. Variation of the velocity distribution functions: $F_d(z,v_z)$ and $F_b(z,v_z)$ in the shock front at $M=8.19$.

bution begins with the generation of high-energy tails. Then the change extends into the region of smaller v_x. In the vicinity of the point $v_x=0$ the distribution remains unchanged until a new equilibrium state is reached. The bimodal approximation describes the evolution of the function $G(z,v_x)$ to a good accuracy.

The transformation of the v_z distribution begins in a similar way: first, the high-energy tail is formed. Then the new (downstream) distribution is formed due to the particle flux in velocity space. It is seen from the results of simulation that the width of the distribution function $F(z,v_z)$ within the shock front is greater than its width in the equilibrium downstream flow. The function $F_b(z,v_z)$ calculated using the bimodal approximation (1) differs little from the function $F_d(z,v_z)$ obtained from the MD simulation. Calculations show, however, that the difference decreases with decreasing Mach number. This fact is inconsistent with the popular point of view that the bimodal distribution affords better approximation at higher Mach numbers, when the shock wave thickness is small. At Mach numbers M close to unity, the functions $f_1(\mathbf{v})$ and $f_2(\mathbf{v})$ are close to each other, and Eq. (1) has correct limit as $M\rightarrow 1$. Figures 1, 2, and 3 clarify the origin of the ''temperature maximum'' observed in some of the previous studies of shock wave structure, and show that the bimodal distribution (1) is close to the real distribution function in shock waves.

In Fig. 4 the evolution of the pair distribution function $N(r)$ (defined similarly to Ref. 16; here r is the vector in the xy plane) across the shock front is shown. In the upstream flow $N(r)$ exhibits a maximum whose position corresponds to the minimum of the interparticle potential $r=2^{1/6}\approx 1.12$. This maximum is less pronounced (but its position does not change) in the downstream flow, where the temperature is much greater than the potential minimum depth ε. Accordingly, the average potential energy per particle is about -0.2 in the upstream region and $+0.007$ in the downstream region.

Within the shock wave front, the velocity distribution function is not spherically

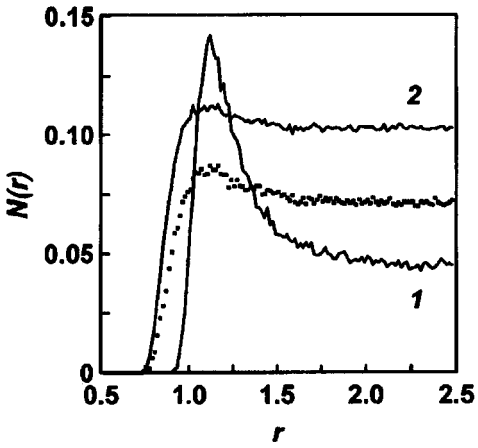

FIG. 4. The pair distribution function in the upstream (*1*) and downstream (*2*) flows, and at the center of the shock layer (dots) at $M=8.19$.

symmetric. The pressure in this case is a symmetric tensor, rather than a scalar. The definition of this tensor in the general nonequilibrium case is given in Ref. 20. If the shock layer is planar (and normal to the z axis), the pressure has diagonal form: $P_{xx}=P_{yy}=P_\tau$, $P_{zz}=P_n$, where P_τ and P_n are the tangential and normal pressure components. The difference between the pressure components at the surface of a macroscopic body gives rise to the surface tension. A similar effect takes place in a shock wave.[21] The surface tension coefficient can be calculated using the formalism of Refs. 20 and 22 as

$$\gamma=\int (P_n-P_\tau)dz.$$

Calculating the pressure components from the MD simulation data yields the surface tension coefficient $\gamma=17.38=250$ dyne/cm at $M=8.19$ and $\gamma=1.232=17.7$ dyne/cm at $M=2.65$. These results are in qualitative agreement with the estimates of Ref. 21. Note that in the case of gases the surface tension is connected with the gas-kinetic pressure, and the coefficient γ is roughly proportional to (M^2-1).

One of the authors (S. A.) is grateful A. I. Larkin for helpful discussions and to the Institute of Laser Engineering, Osaka University for offering a guest position. The work was supported by Russian Fund for Fundamental Research, Grant 95-02-04535a.

[a)]e-mail: basil@landau.ac.ru

[1]L. D. Landau and E. M. Lifshitz, *Fluid Mechanics*, Oxford: Pergamon Press, 1959.
[2]H. W. Liepman, R. Narashima, and M. T. Chahine, Phys. Fluids **5**, 1313 (1962).
[3]D. Gilbarg and D. Paolucci, J. Ratl. Mech. Anal. **2**, 617 (1953).
[4]I. E. Tamm, Tr. Fiz. Inst. Akad. Nauk SSSR **29**, 317 (1965).
[5]H. M. Mott-Smith, Phys. Rev. **82**, 885 (1951).
[6]C. Muckenfuss, Phys. Fluids **5**, 1325 (1962).

[7] W. Fiszdon, R. Herczynski, and Z. Walenta, in *Rarefied Gas Dynamics*, edited by M. Becker and M. Fiebig, Porz-Wahn, DFVLR Pres, 1974, p. B23
[8] S. M. Yen, Annu. Rev. Fluid Mech. **16**, 67 (1984).
[9] G. A. Bird, *Molecular Gas Dynamics*, Oxford: Clarendon Press, 1976.
[10] G. Ya. Lyubarsky, Zh. Éksp. Teor. Fiz. **40**, 1050 (1961) [Sov. Phys. JETP **13**, 740 (1961)].
[11] R. G. Barantsev, Zh. Éksp. Teor. Fiz. **42**, 889 (1962) [Sov. Phys. JETP **15**, 615 (1962)].
[12] W. G. Hoover, Phys. Rev. Lett. **42**, 1531 (1979).
[13] B. L. Holian, W. G. Hoover, and B. Moran, G. K. Straub, Phys. Rev. A **22**, 2798 (1980); B. L. Holian, Phys. Rev. A **37**, 2562 (1988).
[14] M. Koshi, T. Saito, H. Nagoya *et al.*, Kayaku Gakkaishi **55**, 229 (1994).
[15] E. Salomons and M. Marechal, Phys. Rev. Lett. **69**, 269 (1992).
[16] S. I. Anisimov and V. V. Zhakhovskii, JETP Lett. **57**, 99 (1993).
[17] D. W. Heerman, *Computer Simulation Methods in Theoretical Physics*, Berlin–New York: Springer-Verlag, 1986.
[18] V. V. Zhakhovskii and S. I. Anisimov, Zh. Éksp. Teor. Fiz. **111**, 1328 (1997) [JETP **84**, 734 (1997)].
[19] V. A. Rabinovich, A. A. Vasserman, V. I. Nedostup, and L. S. Veksler, *Thermodynamical Properties of Neon, Argon, Krypton, and Xenon*, Berlin – New York: Hemisphere, 1988.
[20] P. Resibois and M. De Lechner, *Classical Kinetic Theory of Fluids*, New York: J. Wiley and Sons, 1977.
[21] A. G. Bashkirov, Phys. Fluids A **3**, 960 (1991).
[22] J. S. Rowlinson and B. Widom, *Molecular Theory of Capillarity*, Oxford: Clarendon Press, 1982.

Published in English in the original Russian journal. Edited by Steve Torstveit.